

University of Louisville

ThinkIR: The University of Louisville's Institutional Repository

Electronic Theses and Dissertations

8-2022

Additive manufacturing of aluminum alloy by metal fused filament fabrication (MF3).

Luke J. Malone
University of Louisville

Follow this and additional works at: <https://ir.library.louisville.edu/etd>



Part of the [Engineering Science and Materials Commons](#), and the [Manufacturing Commons](#)

Recommended Citation

Malone, Luke J., "Additive manufacturing of aluminum alloy by metal fused filament fabrication (MF3)." (2022). *Electronic Theses and Dissertations*. Paper 3927.
<https://doi.org/10.18297/etd/3927>

This Master's Thesis is brought to you for free and open access by ThinkIR: The University of Louisville's Institutional Repository. It has been accepted for inclusion in Electronic Theses and Dissertations by an authorized administrator of ThinkIR: The University of Louisville's Institutional Repository. This title appears here courtesy of the author, who has retained all other copyrights. For more information, please contact thinkir@louisville.edu.

**ADDITIVE MANUFACTURING OF ALUMINUM ALLOY BY METAL FUSED
FILAMENT FABRICATION (MF³)**

By

Luke Malone

Bachelor of Science, Mechanical Engineering, University of Louisville, May 2021

A Thesis

Submitted to the Faculty of the
University of Louisville
J. B. Speed School of Engineering
as Partial Fulfillment of the Requirements
for the Professional Degree

MASTER OF ENGINEERING

Department of Mechanical Engineering

June 2022

**ADDITIVE MANUFACTURING OF ALUMINUM ALLOY BY METAL FUSED
FILAMENT FABRICATION (MF³)**

Submitted by: *Luke Malone*
Luke Malone

A Thesis Approved On

July 1 2022

(Date)

by the Following Reading and Examination Committee:

Sundar Atre

Thesis Director – Dr. Sundar Atre

K-Kate

Dr. Kunal Kate

Gautam Gupta

Dr. Gautam Gupta

I dedicate this thesis to

my fiancée, Emily.

Thank you for your unwavering support, patience, dedication, faith, and joy.

You are my greatest inspiration.

ACKNOWLEDGEMENT

First, I would like to thank Dr. Sundar Atre. I thank him for providing this opportunity to me, meeting with me weekly, and for being a great inspiration to me as a researcher. I would also like to thank Dr. Kunal Kate for guiding me throughout the project; always answering questions, offering insights, and providing encouragement. I also thank Dr. Gautam Gupta for serving on my committee and for offering helpful insights. I would also like to thank Kymera International, including Carrie Barber, Mark Barr, Matteo Zanon, and Tom Pelletiers for the perspectives offered in meetings and conferences.

Additionally, I thank my dear friends in the Materials Innovation Guild, including Kavish Sudan, Saleh Khanjar, Athira Nair Surendran, Benjamin Mitchell, and Sihan Zhang. I must specifically thank Kameswara Pavan Kumar Ajjrapu for his constant guidance and mentorship throughout the project. This group is comprised of the most brilliant and dedicated people I know. It was an honor and privilege to work alongside everyone involved in the Materials Innovation Guild at the University of Louisville.

I also thank all involved in the NASA Kentucky Space Grant Consortium and EPSCoR Programs and the University of Kentucky Office of Sponsored Projects Administration for the wonderful opportunity, including Jacob Owens and Dr. Alexandre Martin.

Additionally, I thank my friends at Techshot, Inc., including Andy Kurk, Rachel Ormsby, Rich Boling, and John Vellinger. Finally, I thank the University of Louisville Speed School of Engineering Department of Mechanical Engineering, including Dr. Stuart Williams, Dr. Ellen Brehob, and Dr. Thomas Berfield.

ABSTRACT

This research studies metal-fused filament fabrication (MF³) for manufacturing aluminum alloy parts. An aluminum alloy powder-based feedstock with a polymer-binder system was extruded via capillary rheometry to form a filament. The filament was used to print green parts that were involved in a two-step debinding process combining solvent and thermal extraction of the polymer binder, then sintered in a partial vacuum. Sintering results including density, shrinkage, and Vickers Hardness were measured to building an understanding of the thermal cycle effectiveness. The main objective is to gain an understanding of the MF³ process characteristics and the ensuing material properties and microstructure through carefully designed experiments, therefore creating additive manufactured components from a common lightweight metal. The overarching goal is to enable rapid, predictable, reproducible, low cost, and accurate production of metal parts with 3D features, thereby significantly expanding the current additive manufacturing capability.

TABLE OF CONTENTS

ACKNOWLEDGEMENT	iv
ABSTRACT.....	v
TABLE OF CONTENTS.....	vi
NOMENCLATURE	vii
LIST OF TABLES.....	viii
LIST OF FIGURES	ix
CHAPTER I. INTRODUCTION.....	1
CHAPTER II. MF ³ PROCESS	6
2.1 INTRODUCTION	6
2.2 GREEN STATE EXPERIMENTAL METHODS.....	13
2.2 GREEN STATE RESULTS AND DISCUSSION	17
2.3 THERMAL STATE EXPERIMENTAL METHODS	47
2.4 THERMAL STATE RESULTS AND DISCUSSION	49
2.5 CONCLUSIONS.....	55
CHAPTER III. SINTERING OF AL-6061 PRINTED PARTS	56
3.1 INTRODUCTION	56
3.2 EXPERIMENTAL METHODS.....	58
3.3 SINTERING RESULTS/DISCUSSION.....	59
2.5 CONCLUSIONS.....	71
CHAPTER IV. CONCLUSIONS/FUTURE WORK	72
APPENDIX I. MF ³ OF 17-4 PH STAINLESS STEEL.....	74
APPENDIX II. MF ³ OF WC-Co.....	78
LIST OF REFERENCES	81
CURRICULUM VITA	85

NOMENCLATURE

A = Mass of sample in air

B = Mass of sample in liquid

d = Average length of indenter mark in Vickers Hardness measurement

F = Force of indenter in Vickers Hardness measurement

HV = Vickers Hardness

ρ = Sintered density

ρ_L = Density of air

ρ_o = Density of auxiliary liquid

LIST OF TABLES

TABLE I	20
TABLE II.....	36
TABLE III.....	36
TABLE IV	39
TABLE V.....	40
TABLE VI	42
TABLE VII.....	43
Table VIII	45
TABLE IX	50
TABLE X.....	62
TABLE XI	65
TABLE XII.....	67
TABLE XIII.....	68
TABLE XIV	69

LIST OF FIGURES

FIGURE 1 - Full MF ³ process diagram.	3
FIGURE 2 - XRD of received aluminum-6061 powder.	17
FIGURE 3 - SEM images of Al-6061 powder, 1500x and 5000x magnification.	18
FIGURE 4 - Initial critical solids loading test of aluminum-6061 feedstock.	24
FIGURE 5 – Second critical solids loading test of aluminum-6061 feedstock.	25
FIGURE 6 - 71 vol% broken filament.	26
FIGURE 7 - Optimum solids loading of 60 vol% aluminum-6061 feedstock.	28
FIGURE 8 - Feedstock batches before and after granulation.	28
FIGURE 9 - Time-dependent viscosity of 60 vol% Al-6061-polymer binder feedstock.	30
FIGURE 10 - Shear rate-dependent viscosity of 60 vol% Al-6061 feedstock.	31
FIGURE 11 - 60 vol% Al-6061 filament with spool diameter of 15 cm.	32
FIGURE 12 - SEM images of 60 vol% Al-6061 filaments. a)1,000x magnification of cross section, b)150x magnification of cross section, c)100x magnification of side profile after loading into a printer.	34
FIGURE 13 - a) 60 vol% Al-6061 filament in printer extruder, b) commonly printed parts including cubes, spheres, and sample tensile bars.	35
FIGURE 14 - Initial DoE Testing SN ratios	37
FIGURE 15 – Refined DoE Testing SN ratios	40
FIGURE 16 - Comparison between initial printing parameters and optimal printing parameters, reducing gaps between layers to create denser green parts	43
FIGURE 17 - Top surface images of printed green part, with R _a of 6.934 μm perpendicular to infill and 5.523 μm along infill	45
FIGURE 18 - Side surface images of printed green part, with Ra of 11.410 μm perpendicular to infill and 5.840 μm along infill	46
FIGURE 19 - Cross section images of printed green part	47
FIGURE 20 - TGA results of feedstock to understand the thermal debinding cycle.	51
FIGURE 21 - TGA results of pure Al-6061 powder	53
FIGURE 22 - Thermal debinding-sintering thermal cycle of solvent debound printed Al-6061 parts.	54
FIGURE 23 - Progression of sintering and polishing pure Al-6061 powder samples	61
FIGURE 24 - Challenges encountered in initial sintering cycles, including loose powder residue, oxidation, and swelling	61
FIGURE 25 - Run 4 sintered samples before and after polishing	66
FIGURE 26 - Kymera sintering tests microstructure images	70
FIGURE 27 - Sintered parts printed with 17-4 PH stainless-steel filament.	75
FIGURE 28 - Redesigned parts using topology optimization technique for future printing	77
FIGURE 29 - WC-Co powder SEM image	79
FIGURE 30 - TGA results of WC-Co feedstocks.	80
FIGURE 31 - Printed WC-Co green part at 25 vol% solids loading	80

CHAPTER I. INTRODUCTION

Metal Fused Filament Fabrication (MF³) is an Additive Manufacturing (AM) process that combines the concepts of Fused Filament Fabrication (FFF), also referred to as Fused Deposition Modeling (FDM), and Metal Injection Molding (MIM). Falling under Material Extrusion Additive Manufacturing (MEAM), MF³ is a growing topic of research and development that is beginning to become more accessible to hobbyists and users in industry, with applications in fields such as aerospace, medicine, and automobiles. MF³ offers many benefits comparable to other AM processes such as electron beam melting (EBM), laser powder bed fusion (LPBF), and Binder Jetting, all of which can reliably produce metal parts. Such advantages for MF³ include the possibility of fabricating metal parts near the full theoretical density, to a point that is comparable to MIM-fabricated parts. These parts are also known to feature more isotropic microstructures and mechanical properties comparable to MIM. MF³ allows access to

complex geometries not normally possible to fabricate using traditional manufacturing routes through methods like generative design. Prototyping of metal parts at comparable mechanical properties and density is more accessible and efficient for MF³ users. The use of FDM printers in MF³ also reduces the handling of loose metal powders, as printing of green parts is done exclusively with filaments and there is no usage of powder beds traditionally used in LPBF, Binder Jetting, and EBM. Lower capital costs are possible for users of MF³, as associated costs would only include purchasing the equipment (printers and furnaces if desired), purchasing of the material (metal powder-polymer binder filaments), and maintenance of the printers. MF³ also allows the possibility of fabricating metal parts in space, as the usage of loose metal powders is not a concern as it is with other types of metal AM. The possibility of reducing the hardware costs on a long-duration crewed mission and greater accessibility to replacing metal parts during the mission also exist. While MF³ is becoming more available, further understanding of the materials and parameters of each step in the MF³ process is still necessary before the process is to become as common as traditional FDM printing of polymers.

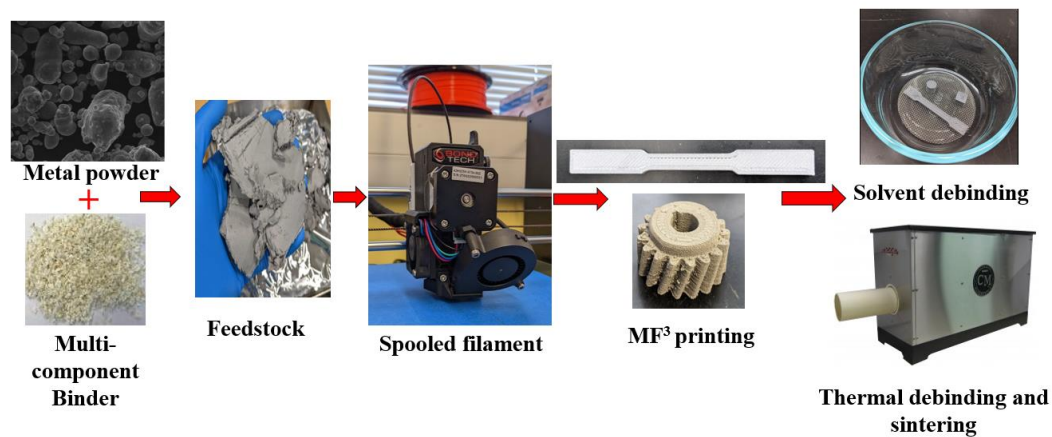


FIGURE 1 - Full MF³ process diagram.

The work presented in this paper covers the entirety of the MF³ process. A full process diagram is shown in FIGURE 1. A metal powder-polymer binder feedstock mixture is formed and extruded into a filament flexible enough to be spooled. The filament is used in a desktop FDM printer to print net shape “green” metal components, still consisting of the metal-polymer binder system. In processing of the printed green parts, a two-step solvent and thermal debinding process occurs. In these two steps, the polymer binder system is dissolved or burned away, leaving a “brown” part consisting of the metal powder components, still holding a net shape structure formed in printing. Sintering of the brown parts in a near-vacuum furnace occurs with the goal of fully densifying and strengthening the printed part. Final characterization of the sintered parts occurs as the final mechanical properties and microstructure are evaluated and compared to MIM standards.

Aluminum-6061 alloy was chosen to be examined for use in the MF³ process. Al-6061 is one of the most common aluminum alloys, used in a variety of industries such as aerospace, automotive, medicine, and more. It is a light-weight metal that offers good corrosion resistance, response to finishing processes, and excellent thermal and electrical conductivities (Fang, 2010). Aluminum powder metallurgy does account for a significant portion of the overall powder metallurgy industry, the latter accounting for 50,000 US tons in the early 2000s (Fang, 2010). There is a great opportunity to utilize aluminum in MF³, increasing the use of the process in more industries and for more applications.

Many parameters must be considered and studied at great length for the successful green printing and debinding/sintering of Al-6061 parts. First, the appropriate powder loading in the metal powder-polymer binder feedstock must be determined to reduce slumping during debinding and shrinkage in sintering. If the loading is too high, inconsistent flow through a printer nozzle could occur, disrupting the homogeneity and structure of a green printed part. Inconsistent homogeneity caused by non-uniform dispersion of the metal powder in the polymer binder can also cause similar issues while printing. Produced filaments must be flexible enough to be handled and to be driven through a printer's extruder. Highly stiff filaments produced at high solids loading of the metal powder will be stiff and brittle, unable to flow through a printer nozzle well enough for consistent printing and possibly breaking within the printer. Additionally, printing parameters, such as nozzle temperature, extrusion width, layer thickness, and print speed must be selected carefully to optimize the green part density. Improper use of the printing parameters can generate voids between printed layers from improper material flow,

resulting in low green density, dimensional warpage, and poor structural integrity. Finally, the debinding and sintering processes must be carefully studied and tested to produce the densest and strongest parts possible. Parameters such as debinding time, sintering temperature, sintering atmosphere, and more are examined to understand their respective effects on fabricating successful aluminum parts. One such factor that would result in unsuccessful part production is the risk of oxidation forming on aluminum part surfaces during sintering. Optimization of the thermal cycle parameters is an essential portion of this study.

Few reports exist that comprehensively examine feedstock and filament characteristics, successful printing parameters, and debinding and sintering outcomes of aluminum-6061 in one process. Therefore, in this work, successful production of metal powder-polymer binder filaments, printing of green parts, and debinding and sintering cycles used to formulate fully dense aluminum-6061 parts that are comparable to other manufacturing processes is reported. CHAPTER II. presents a comprehensive overview of the MF³ process applied to the aluminum-6061 powder-polymer binder material chosen. In this chapter, characterization of the powder, production of the metal powder-polymer binder feedstock and filament, green printing, the two-step solvent and thermal debinding, and initial sintering tests are examined. This work is under preparation for submission in “Additive Manufacturing-Powder Metallurgy Conference”, 2022, Portland. CHAPTER III. SINTERING OF AL-6061 PRINTED PARTS provides an in-depth study of the thermal cycles used to sinter the printed aluminum-6061 printed parts and the following results, including mechanical properties and microstructure.

CHAPTER II. MF³ PROCESS

2.1 INTRODUCTION

In this work, aluminum-6061 alloy was selected as the metal powder used in the produced feedstocks. Aluminum, especially the 6061 alloy, is featured in almost any industry that makes use of metal parts, including the aerospace, medicine, and automotive industries, which can require intricate geometries with requirements regarding the material's mechanical properties. Aluminum alloys are commonly utilized in Metal Injection Molding (MIM) production process, which can accomplish the manufacturing of the oftentimes small and precise geometries required by the complex applications in those industries (German & Metal Powder Industries Federation., 2011). As Metal Fused Filament Fabrication (MF³) shares many similarities with the MIM production process, utilizing aluminum filaments in MF³ to print and debind/sinter parts comparable to those

produced in MIM is a topic of great interest and study. In this chapter, each step of the MF³ process is studied through the production of the aluminum-6061 powder-polymer binder feedstock filaments, printing of green parts, two-step solvent and thermal debinding, and sintering to form final parts. This further validates the MF³ process, applying another metal alloy in each of the steps to prove its effectiveness and future use.

In the open literature, it is clear to see that the MF³ itself process is undergoing great study and review. Many other materials are being evaluated and applied to MF³, including WC-Co and 316L Stainless Steel (José et al., n.d.), (Thompson et al., 2019). Cerejo et al. developed WC-Co filaments at various solids-loadings to print green parts that were debound and sintered. The final filament consisted of 48.5 (vol%) of WC-10Co and fulfilled the requirements of flexibility and strength. Final sintered parts featured Young's Modulus of 678 ± 72 GPa ($98.3 \pm 10.4 \cdot 10^6$ psi), proving the capabilities of the MF³ process to produce strong metal parts (José et al., n.d.). Thompson et al. developed 55 vol% 316 L stainless steel filaments that were used to print green parts. Sintering at 1360°C (2480°F) after solvent and thermal debinding resulted in parts with 95% relative density and isotropic shrinkage of 20% that were comparable to rolled sheet material in strength tests (Thompson et al., 2019). These papers further validate the MF³ process, shown in FIGURE 1 used in this study to fabricate complex and dense parts out of a wide variety of metal materials.

Using aluminum-6061 filaments to print green parts is a topic that is not yet fully investigated in the wider literature. Therefore, much work in this study was done to prove

the concept of using the produced aluminum-6061 filaments to successfully print 3D geometries. If no current framework exists to provide proper settings and conditions needed to ensure successful printing with the new filament material, much investigation is then required. While the open literature did not contain studies focused on printing green parts from aluminum-6061 filaments, there were many papers that conducted printability experiments on other new filament materials. To improve the dimensional accuracy of parts printed on a traditional Fused Deposition Modelling (FDM) printer, also used in the MF³ process, Schneidler et al. used the Design of Experiments (DoE) approach to select the ideal processing parameters to produce the desired level of reproducibility. The DoE statistical approach combined parameters such as the feed rate, extrusion temperature, layer thickness, and flow rate through the extruder nozzle and analyzed the correlation that would achieve the best dimensional accuracies (circular, angular, and linear) and surface finishes in parts printed out of polylactic acid (PLA). The slowest feed rate, greatest flow rate, and lowest layer thickness led to the best parts (Schneidler et al., 2021). In another study by Pazhamannil et al., a similar statistical approach via Taguchi Analysis DoE compared process parameters such as print speed, layer thickness, nozzle temperature, and fan speed on the printed parts' mechanical properties such as yield strength and Elastic Modulus across several commonly used polymers in FDM printing (Pazhamannil et al., 2022). The DoE approach to analyzing the optimal printing conditions certainly applied to MF³ in particular, shown in a study by Godec et al. The DoE approach was used to find the ideal extrusion temperature, flow rate multiplier, and layer thickness for printing with 17-4PH Stainless Steel-polymer

composite filaments that would optimize the tensile strength and modulus. Highest flow rate multiplier, nozzle temperature, and increased layer thicknesses led to the improved mechanical properties (Godec et al., 2020). To further improve the mechanical properties of parts printed out of a Ti-6Al-4V powder-polymer binder composite, Taguchi Analysis DoE was used to find the optimal printing conditions to produce the parts with the highest green density, lowest dimensional variation, and lowest surface roughness. Green density was used as a response parameter in the study, as higher green densities lead to higher sintered densities and therefore improved mechanical responses (Singh, Balla, Atre, et al., 2021). It was seen that increasing the flow rate of material through the printer extruder nozzle deposits more material per layer, increasing the green density with greater effectiveness than other parameters (Singh et al., 2020). In this work, a Taguchi Analysis DoE is conducted that measures the correlation between nozzle temperature, layer thickness, and print speed on producing higher green densities with the aluminum-6061 feedstock filament, with the effects on nozzle size and extrusion multiplier also being studied.

Another great challenge examined in this study is the successful sintering of printed aluminum-6061 parts. While the use of aluminum-6061 filaments in MF³ is scarce in the literature, much of the research on aluminum AM is focused on processes such as LPBF (Uddin et al., 2018). Meanwhile, it was seen that many studies have been conducted on the sintering of aluminum. From the open literature, a framework was established to serve as a starting point for sintering the debound Al-6061 printed parts.

The heating rates chosen for testing are in a range that is not considered to be rapid heating. Traditionally, rapid heating approaches feature many benefits such as reduced grain growth and greater diffusion activation from more enhanced thermal gradients but limit the amount of control allowed and can lead to greater distortion and cracking. Also, the approaches needed for rapid heating, such as flash heating or microwave heating, are not included with the chosen furnace (German, n.d.). In initial sintering experiments of the aluminum-6061 alloy powder by Kymera International, the supplier of the powders used in this work, a heating rate of 2 °C/min to a sintering temperature at 625 °C for 2 hours was used (Kymera International, Durham, North Carolina). The heating rate range and hold time chosen are also derived from previous studies involving sintering aluminum compacts with similar powder characteristics (Schaffer & Hall, n.d.) (Wu et al., 2021) (Liu et al., 2007) (Schaffer et al., 2006).

Nitrogen was chosen as the ideal sintering atmosphere, which is one of the most beneficial atmospheres to use when sintering aluminum. Aluminum powder is known to oxidize during sintering, and nitrogen is widely regarded as the most suitable furnace atmosphere compared to other gases such as argon. Schaffer et. al. sintered three aluminum alloys using argon and nitrogen atmospheres. In this study, nitrogen was proven to be the most effective sintering atmosphere due to the greater pore filling and densification (Schaffer & Hall, n.d.). When sintering under a nitrogen atmosphere, the aluminum reacts with the gas and aluminum nitride begins to form (Fang, 2010) (Kent et al., 2010). Aluminum nitride reduces the pressure in pore spaces, allowing liquid pore filling to occur during densification, resulting in less porosity. Samples sintered in

nitrogen are generally less porous due to the liquid pore filling (Schaffer et al., 2006). Additionally, a nitrogen atmosphere is known for sintering aluminum parts with higher sintered strengths compared to other atmospheres (Fang, 2010). In a study by Schaffer et al. which compared sintering aluminum powder compacts under different atmospheres, nitrogen atmospheres consistently produced parts with the highest densification, proving the consistency and repeatability of the atmosphere (Schaffer et al., 2006). Nitrogen was also used as the atmosphere in initial sintering tests conducted on the aluminum-6061 alloy powders by Kymera International, the supplier of the powders used in this work (Kymera International, Durham, North Carolina). When sintering under any atmosphere, a low dew point is desired, with the range of -51°C to -40°C being ideal (Fang, 2010). The presence of moisture can produce hydrogen, causing the formation of aluminum hydride and can prevent liquid pore filling due to hydrogen's high solubility in aluminum (Schaffer et al., 2006).

In many studies, additives are supplemented to the sintering of aluminum to form aluminum alloys for an improved sintering response. Such additives can include magnesium, copper, zinc, and tin. The powder used in the production of the metal powder-polymer binder feedstock in this study contains a wide variety of other elemental additives, as the powder is an aluminum-6061 alloy, leading to a high possibility of liquid phase sintering occurring. The presence of liquid phases in the sintering of the aluminum alloy will be beneficial, leading to greater densification and sintering results (Schaffer et al., 2001).

While these papers provide a good framework used in initial testing, other studies prove the challenges that exist in metal powder sintering. Challenges in sintering aluminum powder include low densification, oxidation, and porosity, and a review was conducted to investigate how such challenges were addressed in the microstructure and performance of similar materials. In a study by Yang et al., the effect of sintering temperature on pore morphology, porosity, and mechanical behavior of porous titanium foams was examined. When the sintering temperature increased from 900 °C to 1200°C, porosity decreased from 56.48% to 46.83% and the yield strength increased from 101.81 to 208.01 MPa. While the porosity was still higher than what is desired for this study, a potential approach to decreasing porosity by increasing the temperature is introduced (Yang et al., 2021). Additionally, in a study by Chen et al., Al-doped ZnO samples were sintered via Spark Plasma Sintering (SPS) and compared to those sintered via a conventional method. The incorporation of the Al ions in the ZnO introduced structural distortions but high electrical conductivity was still achieved, proving that good properties can still come from parts with distortions in the microstructure (Chen et al., 2020). In a study by Soares et al., AA7075 aluminum alloy powder samples were sintered by SPS as-received or after ball-milling. It was seen that in the sintered ball-milled powder samples, there were greater dislocation densities but also a greater yield strength. Although the ball-milled samples featured more imperfections, it still performed better than the other type of sample, showing that imperfections in the material's microstructure can still lead to benefits (Soares et al., 2021). In a similar study, aluminum powder samples were sintered either with no additional operations or after mechanical milling,

which can result in microstructure refinement (nanocrystalline or ultrafine-grained). To retain the finer microstructures, samples that were milled were sintered high frequency induction sintering (HFIS) at short sintering times yielded better mechanical properties, showing that microstructure differences can still lead to benefits (Mendoza et al., 2021). These papers highlight challenges that can exist in sintering metal powder samples, especially in aluminum, but there are still solutions for greater densification and even advantages in the mechanical properties that can exist in samples with voids, distortions, or defects.

In this chapter, aluminum-6061 powder-polymer binder feedstocks are produced, extruded into filaments, and used to successfully print 3D dense green parts. After a two-step solvent and thermal debinding process, the parts are sintered in a nitrogen atmosphere for densification. This chapter proves the concept of using the aluminum-6061 alloy filaments in MF³ process to form complex geometries with results comparable to those produced using MIM.

2.2 GREEN STATE EXPERIMENTAL METHODS

The present work uses an aluminum-6061 alloy powder with a median particle size of 37 μm (Kymera International, Durham, North Carolina). Upon receiving the powder, characterization tests were performed to better understand the powder's effect on flowability during printing and packing density in the feedstock. The true density of the powder was measured using a helium gas pycnometer (Accupyc II 1340, Micromeritics

Inc., GA, USA). The apparent density of the powder was measured by filling a graduated cylinder to a chosen volume, then dividing the volume value by the mass of the powder. Per ASTM B527-15, the powder's tap density was determined by using a tap density volumeter (AS-100 Tap Density Tester, Aimsizer Scientific, Dandong Liaoning, China). To confirm the composition of the received alloy, the constituent phases of the pure powder were identified by analyzing the X-Ray Diffraction (XRD) pattern (Discovery D8 HR, BRUKER AXS, Inc., USA). Powder samples were also analyzed under a Scanning Electron Microscope (SEM) (TESCAN Vega3 SEM, TESCAN Inc., Brno, Czech Republic) to confirm particle shape and size.

The feedstock used to produce the flexible filaments for printing is made of the solid metal powder and four polymers making up the binder system. The binder system consists of two backbone polymers, an elastomer, and a plasticizing phase. The backbone polymers allow the filament to be strong and stiff enough to be extruded through an FDM printer. They also assist the green part in retaining its structure after thermal debinding, else the component would not be able to hold the printed geometry. The elastomer provides flexibility to the filament, allowing it to be spooled into a circular form after extrusion (Wagner et al., 2022). This is essential for successful printing, as filaments that are too stiff cannot be extruded well through the printer's extruder. The circular form of the filament allows it to be mounted on the side or top of the printer, allowing continuous flow of the material through the printer's extruder without constant maintenance. The plasticizing phase lowers the viscosity of the feedstock, allowing the produced filament to flow more easily through the printer's nozzle.

Solids loading of the feedstock was experimented on by blending the metal powder-polymer binder system together in a torque rheometer (IntelliTorque Plasti-Corder, C. W. Brabender Instruments, Inc. NJ, USA). After many experiments determining the critical solids loading of the metal powder-polymer binder feedstock, an optimum solids loading point was found, which was used in further experiments and work. Produced feedstocks were loaded in a plastic chopper (Col-Int Tech, South Carolina, USA) to granulate the feedstock into pellets. Viscosity measurements of the granulated feedstock pellets were performed using a capillary rheometer (Rheograph 20, GÖTTFERT Werkstoff-Prüfmaschinen GmbH, Germany). A tungsten carbide die (L/D ratio of 30:1) was used in the viscosity measurements to extrude the feedstock through the rheometer. Time-dependent viscosity was first measured, whereas the pelletized feedstock was extruded through the tungsten carbide die with a constant shear rate of 50 s^{-1} and constant temperature of 160°C . By analyzing the variations in viscosity, the feedstock's homogeneity was measured. Two shear rate-dependent viscosity tests were performed with the pelletized feedstock at 200°C and 220°C to understand the effect of shear rate and temperature on the feedstock's viscosity. The pelletized feedstock's true density was also measured with the helium gas pycnometer. When measuring the density, random samples were selected from within the produced batch to ensure feedstock homogeneity and consistency in the data.

The feedstock was extruded into a filament using the capillary rheometer. Each extruded filament had a diameter of $1.75 \pm 0.05 \text{ mm}$ via a tungsten carbide die (L/D ratio of 30:1.75). Every filament was extruded at a constant temperature of 110°C and speed of

0.1 mm/s, with the force required to extrude the filament through the die not exceeding 9 kN. Filament cross-section and side profiles were imaged under SEM to better understand the material's homogeneity, the smoothness of the filament, and how well the filament could be passed through a printer's extruder without getting too damaged. The filament's true density was also measured with the helium gas pycnometer, with samples being taken from multiple locations to ensure material homogeneity and consistency in the data.

Green parts were printed using a standard FDM printer (Prusa i3 MK3S+ Printer, Prusa Research by Josef Prusa, 17000 Prague 7, Czech Republic) with an upgraded extruder (BMG Extruder, Bondtech, Värnamo, Sweden). The upgraded extruder featured a higher gear ratio of 3:1 that allowed extra force for the filament to overcome the pressure drop needed to flow through the nozzle. The extruder featured a side thumb screw that could be adjusted to increase or decrease the force acting on the filament to flow through the nozzle, making it ideal for printing with metal filaments. A Taguchi Analysis Design of Experiments (DoE) statistical analysis on Minitab software (Minitab, LLC, State College, Pennsylvania, USA) was conducted to correlate printing parameters including extruder temperature, print layer thickness, and print speed to highest green density achievable. The optimized parameters were a 210°C nozzle temperature, 0.25 mm layer height, and 10 mm/s print speed. Other parameters used during printing included a bed temperature of 65°C, brass nozzle diameter of 0.6 mm, and extrusion multiplier of 1.2. Surface roughness's of the printed parts were analyzed using a surface profilometer (Surftest SJ-210, Mitutoyo, Kanagawa, Japan) and printed parts were

imaged under a Scanning Electron Microscope (SEM) (TESCAN Vega3 SEM, TESCAN Inc., Brno, Czech Republic).

2.2 GREEN STATE RESULTS AND DISCUSSION

FIGURE 2 shows the XRD peaks of the received aluminum-6061 powder. The location of the intensity peaks corresponds with peak locations commonly seen for aluminum-based alloyed powders (Wu et al., 2021). FIGURE 2 confirms that the powder mostly consists of elemental aluminum, with all other alloying elements making up an insignificant portion of the weight.

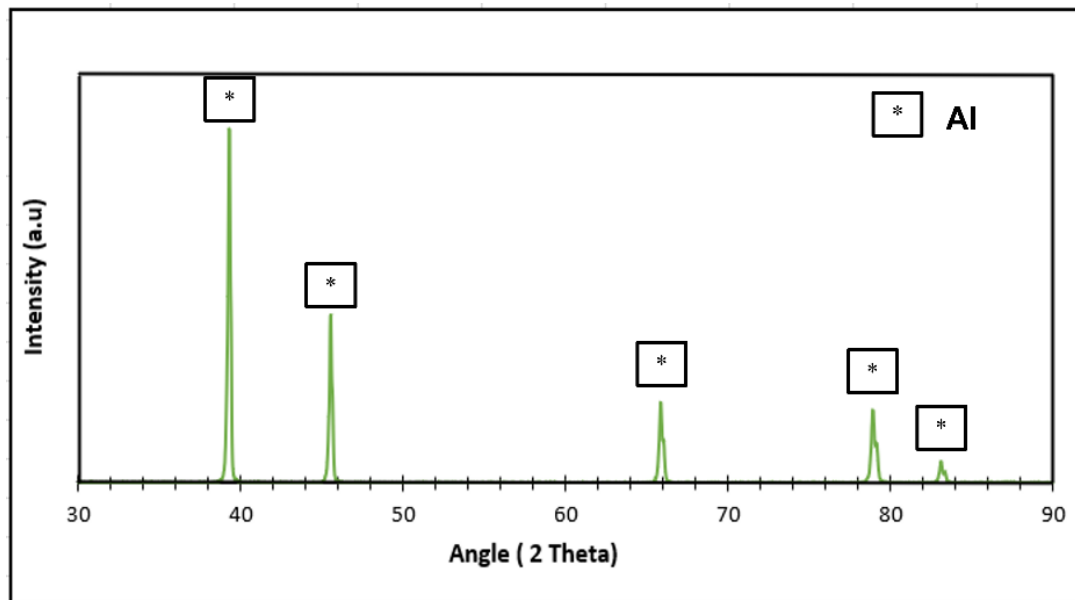


FIGURE 2 - XRD of received aluminum-6061 powder.

FIGURE 3 shows SEM images of the received aluminum-6061 powder. These images, taken at 1500x (left) and 5000x (right) magnification, show the particle sizes and

morphologies of the powder that were used to form the filaments used in printing. The particle size reported by the manufacturer (Kymera International, Durham, North Carolina) is proven by the SEM images. The mostly spherical morphology of the powder is also seen in FIGURE 3, with some powders featuring an elongated shape, especially in the image taken at 5000x magnification (right). Understanding the shape of the particles can lead to a better understanding of how the powder particles will compact together and flow during printing. While it is possible for some non-spherical powders to lead to more dense parts (Liu et al., 2007), it is generally accepted that spherical powders lead to better packing density and flowability (Singh, Balla, Gokce, et al., 2021), as most MIM parts are made using spherical powders (German & Metal Powder Industries Federation., 2011).

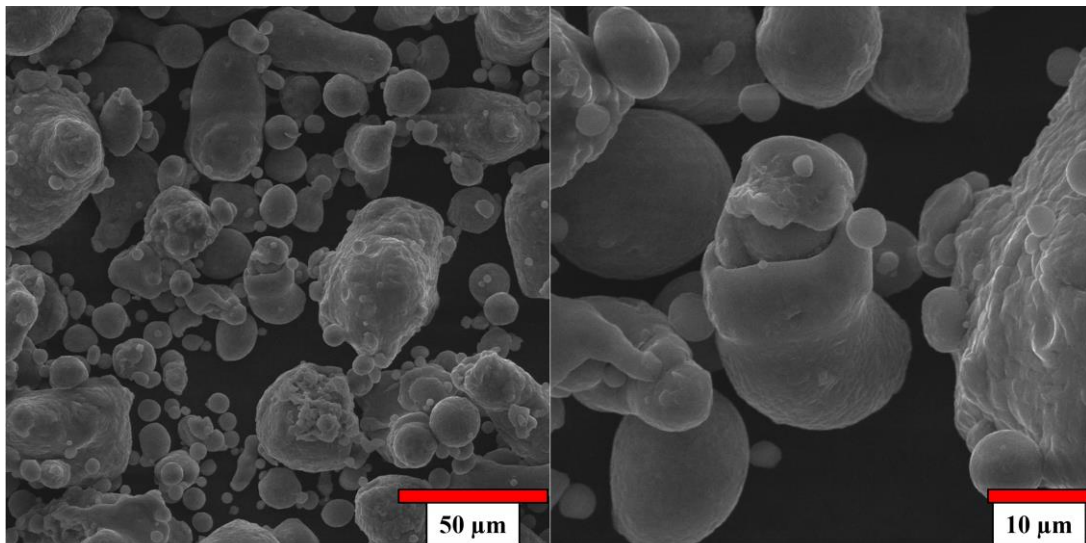


FIGURE 3 - SEM images of Al-6061 powder, 1500x and 5000x magnification.

Seen in FIGURE 3, the particles' diameter ranges from $<10\ \mu\text{m}$ to near $50\ \mu\text{m}$. This is in line with the manufacturer's reported particle sizes, reported in TABLE I, with 10% of the particles having a diameter $<13.2\ \mu\text{m}$ and 90% of the particles having a diameter $<55.3\ \mu\text{m}$. Initial density measurements and powder packing calculations are also shown in TABLE I. The Powder Packing Fraction, found to be 0.66, is the result of dividing the apparent density by the pycnometer density. This ratio indicates the powder's ability to pack together, and as it is greater than 0.60, it shows that the powder can pack well. With good packing, metal powder can fill up more mass in a volume, allowing good addition into the powder-binder feedstock. The Hausner ratio, calculated to be 1.13 indicates the powder's flowability and is calculated by dividing the tap density by the apparent density. As Hausner ratio less than 1.2 indicates that the unpacked powder does not have a mass high enough to decrease resistance to flow (Singh, Balla, Gokce, et al., 2021). It is desirable for the filament formed by the powder-polymer feedstock to have a low viscosity to allow consistent flow through a printing nozzle, and this ratio allows a look into how the metal powder will fill up an unpacked volume, not accounting for too much of the total mass and creating more flow resistance.

TABLE I
POWDER CHARACTERIZATION PARTICLE SIZE AND DENSITY
MEASUREMENTS

Particle Size D10 (μm)	13.2
Particle Size D50 (μm)	37
Particle Size D90 (μm)	55.3
Pycnometer Density (g/cc)	2.71
Tap Density (g/cc)	1.78
Measured Apparent Density (g/cc)	1.58
Powder Packing Fraction (TD/PD)	0.66
Hausner Ratio (TD/AD)	1.13

Understanding the particle size and packing characteristics also allows for a better understanding of the parameters needed in sintering. For larger powders, a higher sintering temperature is needed (Jiang et al., 2021). As smaller particles are compacted together, there are more contacts and opportunities for neck growth at the onset of sintering. Diffusion distances are also decreased with smaller particles, making the diffusion process of particles joining together to form a single body easier. If a powder

compact has a high density, then better diffusion results will follow, leading to higher sintered densities (German, n.d.).

Metal powder-polymer binder feedstocks were produced via torque rheometry at many solids loading points to determine the critical solids limit. Once the critical solids point was determined, an appropriate optimal solids loading point was determined for future feedstocks to be made. Determining the appropriate amount of metal powder in the feedstock is crucial to successfully printing with the feedstock filaments. If there exists too much metal powder in the feedstock, creating a case of high solids loading, printability issues can arise from increased viscosity of the material. At this excessive solids loading, the increased weight percentage from the metal powder causes flow obstructions in the printer's nozzle and incomplete filling with material of the printed part (Singh, Balla, Gokce, et al., 2021). Additionally, filaments with higher metal solids loading are very brittle, breaking very easily when handled. Filaments that are too stiff due to high metal powder solids loading are not ideal for printing, as they will be more prone to breaking in the printer's extruder due to the forces required to move through the nozzle, and flowability through the nozzle required for printing will not exist. If too low of a solids loading point is used in feedstock production, greater shrinking of the printed part during debinding and sintering can occur, as a greater amount of polymer binder is present and will dissolve/burn away. When this occurs, slumping of the final part follows (Singh, Balla, Gokce, et al., 2021). To determine the critical solids loading point, an initial test is conducted whereas a low solids loading point is determined and mixed in the torque rheometer. During mixing, the solids loading of the metal powder increases in 1%

increments with the appropriate amount of powder being manually added to the blended mixture. The mixing torque of the rheometer's rollers is continuously monitored, as it is a measure of the homogeneity of the feedstock blend. With consistent torque readings, the feedstock in the chamber is mixed sufficiently to be considered homogeneous, whereas each metal powder particle is sufficiently coated with the polymer binder. This addition of the metal powder in 1 volume percentage increments continues until there is a great rise in the mixing torque that does not level out or more than 80% of the rheometer chamber volume is filled. When the mixing torque abruptly increases at a critical solids loading point, it is determined that the mixture does not contain enough of the polymer binder system to satisfactorily coat every metal powder particle, causing the mixture to not feature ideal homogeneity and have greater inter-particle friction from increased direct powder contacts (Singh, Balla, Gokce, et al., 2021).

FIGURE 4 shows the mixing torque versus time graph from the first critical solids loading test that was conducted with the aluminum-6061 metal powder-polymer binder feedstock mixture. FIGURE 4 also shows the torque versus solids loading graph resulting from the torque versus time plot. This plot allows the "slope" of the torque to be clearly seen at each volume percentage increment. In this initial critical solids loading test, a starting solids loading of 55 % by volume (vol%) of the aluminum-6061 powder was selected. In increments of 1 vol%, powder was added until 69 vol% was reached. The mixing torque initially stabilized at around 15 Nm and finally evened out at around 35 Nm at the final solids loading. As seen in FIGURE 4, the mixing torque increased by about 1 Nm every 1 vol% of metal powder. In this test, there were no abrupt changes in

the mixing torque, as the change in mixing torque follows a linear increasing slope. However, the maximum solids loading amount for the test, 69 vol%, is traditionally very high for metal powders. Another test, shown in FIGURE 5, was conducted at higher solids loading to find a clearer critical solids loading point. FIGURE 5 shows the torque versus time graph and the result torque versus solids loading amount. The starting loading was 69 vol% and the test ended at 79 vol%, both points being very high solids loading amounts. This test followed a similar pattern shown in FIGURE 4, with the mixing torque initially stabilizing at 15 Nm and finally evening out at around 35 Nm at the final solids loading, with the mixing torque increasing by about 1 Nm every 1 vol% of metal powder.

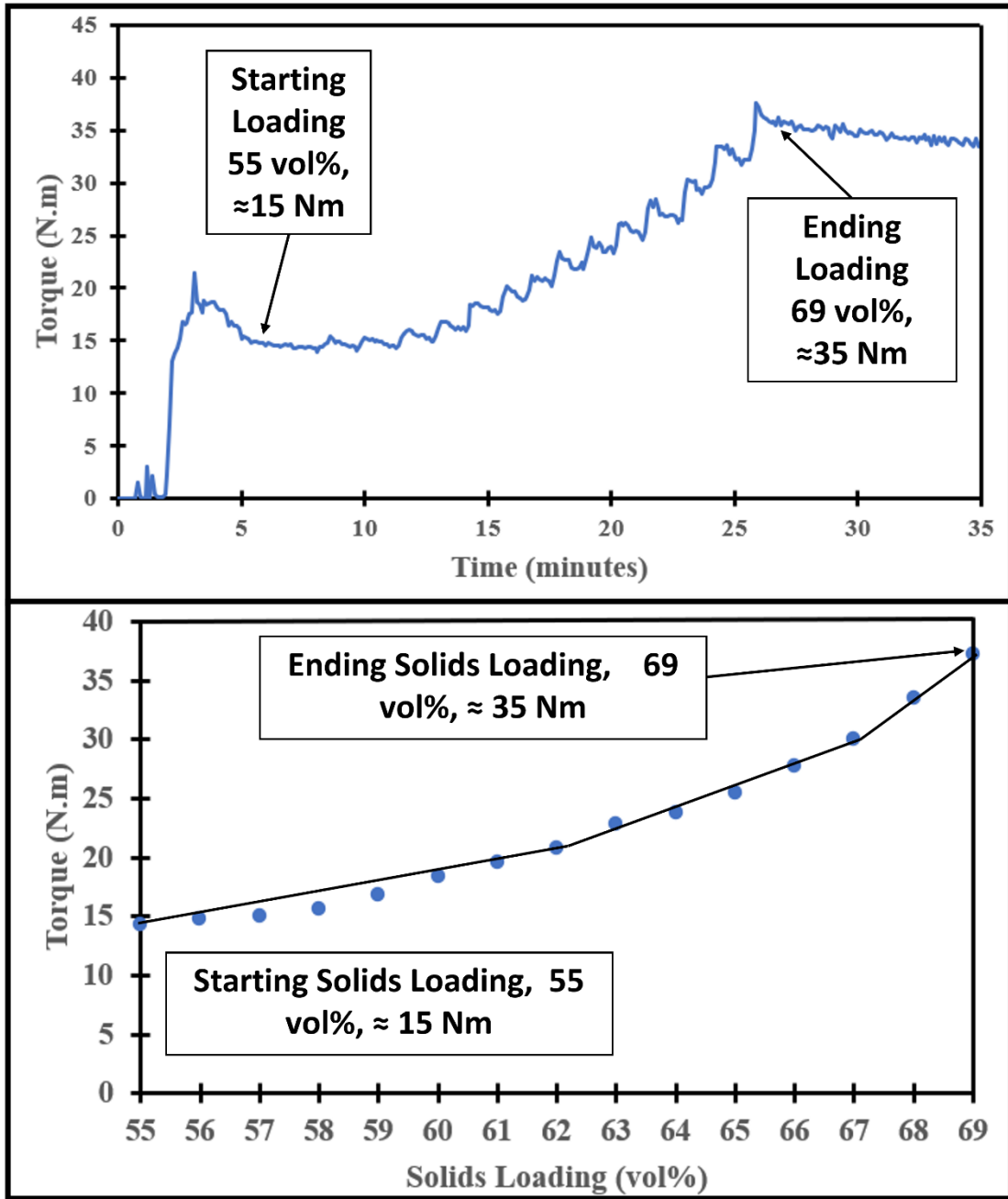


FIGURE 4 - Initial critical solids loading test of aluminum-6061 feedstock.

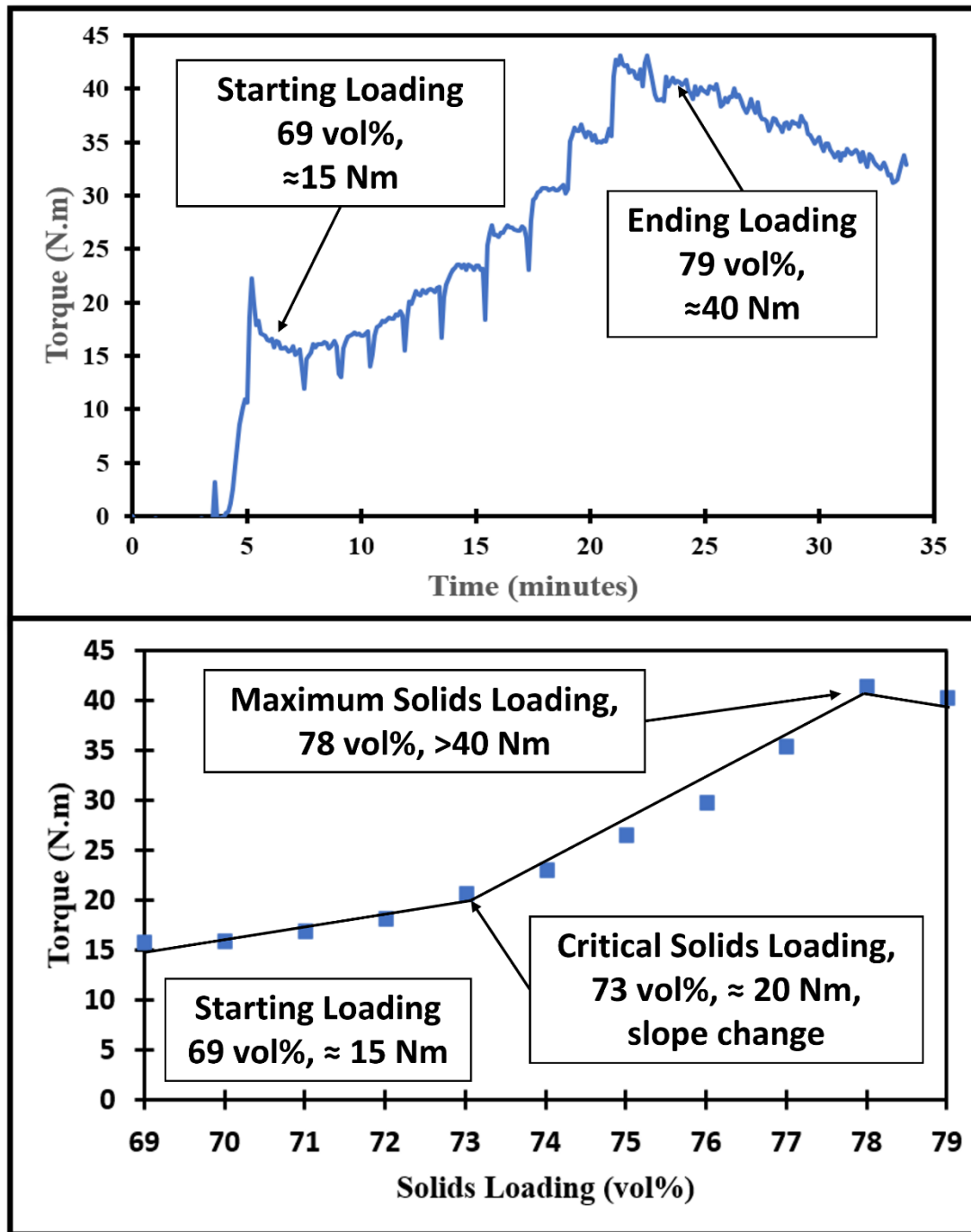


FIGURE 5 – Second critical solids loading test of aluminum-6061 feedstock.

In FIGURE 5, the critical loading point was shown to be 73 vol%, when the rate of torque increase per solids loading greatly increased. At this point, it was decided that too much of the metal powder was in the feedstock and would result in brittle filaments, whereas the metal powders would not be uniformly coated with the polymer binder system. To prove that the critical solids loading point would be too high in producing successful filaments, a feedstock was produced at 71 vol%. The filament extruded from that feedstock batch was very brittle, breaking very easily when handling, as shown in FIGURE 6. No other filament was produced using this solids loading amount, as it was proven that too high of a solids loading results in brittle filaments that would not be suitable for successful printing. This filament would not have been able to be passed through a printer's extruder and nozzle without breaking and was not used in any printing experiments. Therefore, a lower solids loading amount was chosen at 60 vol% and used in future feedstock filament production.



FIGURE 6 - 71 vol% broken filament.

FIGURE 7 shows the mixing torque versus time graph for the production of the optimum solids loading feedstock (60 vol%). While there was a great torque value in the beginning of the test, it is clear that the mixing torque stabilizes at around 22 Nm. In this test, no additional metal powder was added to the feedstock, so there should not be any direct increases in the mixing torque. It was determined that the resulting feedstock was homogeneous and ready for filament production since the mixing torque remained constant for the duration of the mixing after it was loaded, being almost 25 minutes.

When the feedstock is initially blended, it is formed into large pieces that are difficult to break off. To make loading of the feedstock into the capillary rheometer possible, the feedstocks were ground down into pellets. FIGURE 8 shows the feedstock after being mixed in the torque rheometer and a sample of the granulated feedstock pellets.

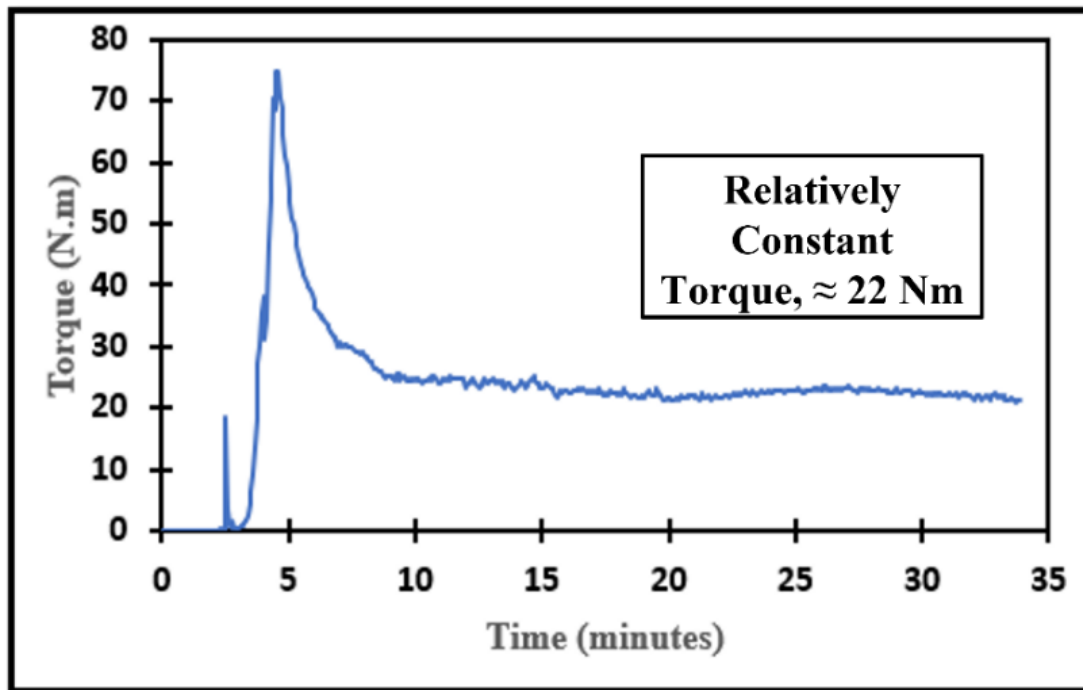


FIGURE 7 - Optimum solids loading of 60 vol% aluminum-6061 feedstock.



FIGURE 8 - Feedstock batches before and after granulation.

The time-dependent viscosity for the 60 vol% Al-6061-polymer binder feedstock pellets was determined at 160°C and a constant shear rate of 50 s⁻¹ in the capillary rheometer barrel. FIGURE 9 shows the resulting plot. The feedstock features a viscosity of 840 ± 44 Pa.s, being relatively constant with respect to time. This measurement gives insight into the homogeneity of the feedstock, as homogeneous feedstocks will have a consistent viscosity with time at a constant shear rate. This measurement proves that the feedstock was blended well in the torque rheometer and theoretically contains the same proportionate amount of metal powder and polymer binder in each sample of the batch. This time-dependent viscosity measurement is applicable for printing with the filaments produced from the feedstock, as consistent material extrusion and uniform distribution of the metal powder across the printed part are desirable. If feedstock filaments are inconsistent in powder distribution, slumping or uneven distortion can occur in printed and sintered parts.

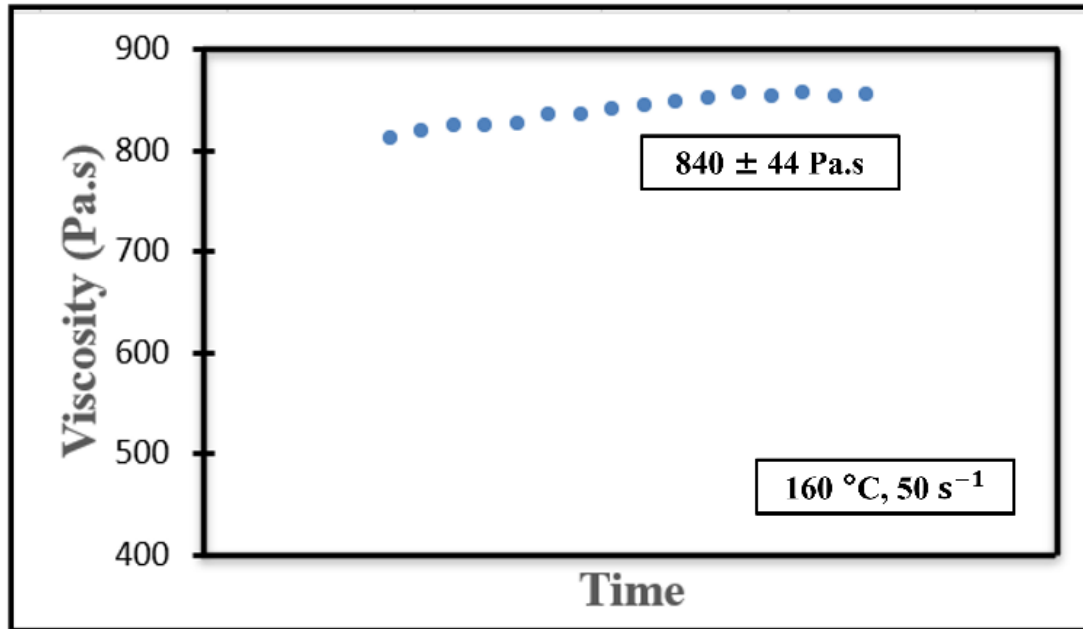


FIGURE 9 - Time-dependent viscosity of 60 vol% Al-6061-polymer binder feedstock.

The shear rate-dependent viscosities 60 vol% Al-6061 powder-polymer binder feedstock pellets were determined at temperatures of 200 °C and 220 °C with increasing shear rates in the capillary rheometer barrel. FIGURE 10 shows the resulting measurement. For the 220 °C measurement, the viscosity of the feedstock began at 189 Pa.s at 16s^{-1} and ended at 8 Pa.s. at 1306s^{-1} . For the 200 °C measurement, the viscosity of the feedstock began at 293 Pa.s at 10s^{-1} and ended at 87 Pa.s. at 943s^{-1} . For both measurements, the viscosity of the feedstock decreased with increasing shear rates. The 220 °C measurement featured lower viscosities compared to the 200 °C measurement. This test proves that with an increase in temperature, the feedstock will have a lower viscosity. This is applicable to printing green parts with the filament produced from the feedstock, as low viscosity is desirable for the material to suitably flow through the

nozzle. 200 °C and 220 °C were chosen as the temperatures for the two tests as those were two of the nozzle temperatures tested when determining the ideal printing settings.

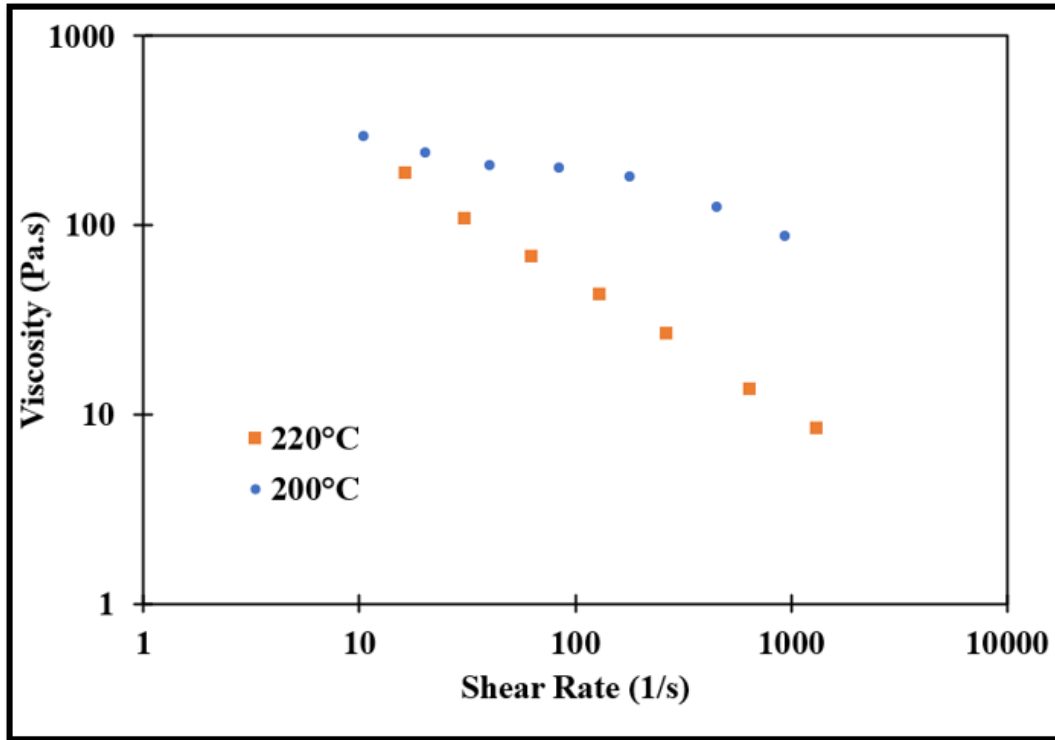


FIGURE 10 - Shear rate-dependent viscosity of 60 vol% Al-6061 feedstock.

The green filaments were extruded from the capillary rheometer at 110 °C and 0.1 mm/s, using a feedstock with the 60 vol% solids loading. Filaments at this solids loading proved to be more flexible than the filament produced at the higher solids loading of 71 vol%, shown in FIGURE 6, and was able to be used in future printing experiments, not breaking in the printer's extruder during material extrusion. Proving the filament's flexibility, it was able to be spooled with an inner diameter of ≈ 15 μ m, shown in FIGURE 11.



FIGURE 11 - 60 vol% Al-6061 filament with spool diameter of 15 cm.

FIGURE 12 shows three images of the filament produced with 60 vol% Al-6061 powder. FIGURE 12a and FIGURE 12b show images of the filament's cross section. FIGURE 12a features a magnification of 1000x, showing the polymer binder and metal powder matrix, with the polymer binder adhered to the spherical powder particles. FIGURE 12b features a magnification of 150x, showing the circular profile that is seen in all filaments. From here, it is clear to see the filament's homogeneity, with the polymer binder mixed with the Al-6061 powder and evenly spread across the whole cross section. This uniform distribution is expected to enable uniform flow through the printer's nozzle and consistent properties in printed parts. FIGURE 12c shows a side profile at 100x magnification of a filament previously loaded through a printer's extruder. The

smoothness of the surface, with only a few notches present resulting from the gears of the extruder contacting the filament, shows the effectiveness of the filaments when passing through a printer. This proves the filaments' strength and flexibility, allowing them to be easily loaded into and unloaded from a printer's extruder and retaining consistent features and surface properties. While there are defects present from the extruder gears, shown in FIGURE 12c, they do not greatly impact the filament's printability, as many parts were able to be printed with the 60 vol% filaments. FIGURE 13 shows the filament loaded in the Prusa i3 MK3S+ FDM printer as well as sample parts that were printed using the 60 vol% filaments. The filament featured excellent flowability through the printer's nozzle, able to print the parts layer-by-layer with no major inconsistencies between layers or across part cross sections.

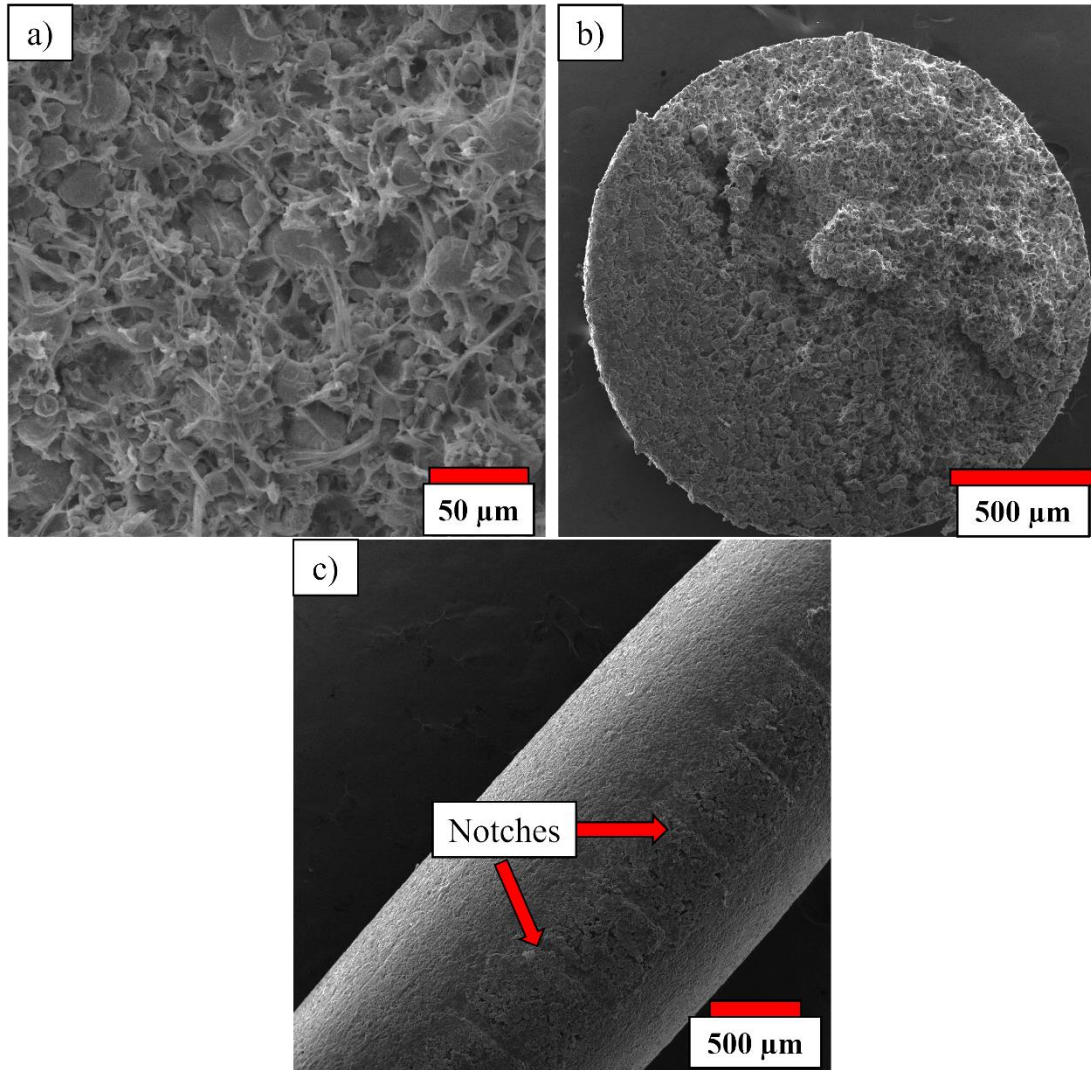


FIGURE 12 - SEM images of 60 vol% Al-6061 filaments. a)1,000x magnification of cross section, b)150x magnification of cross section, c)100x magnification of side profile after loading into a printer.

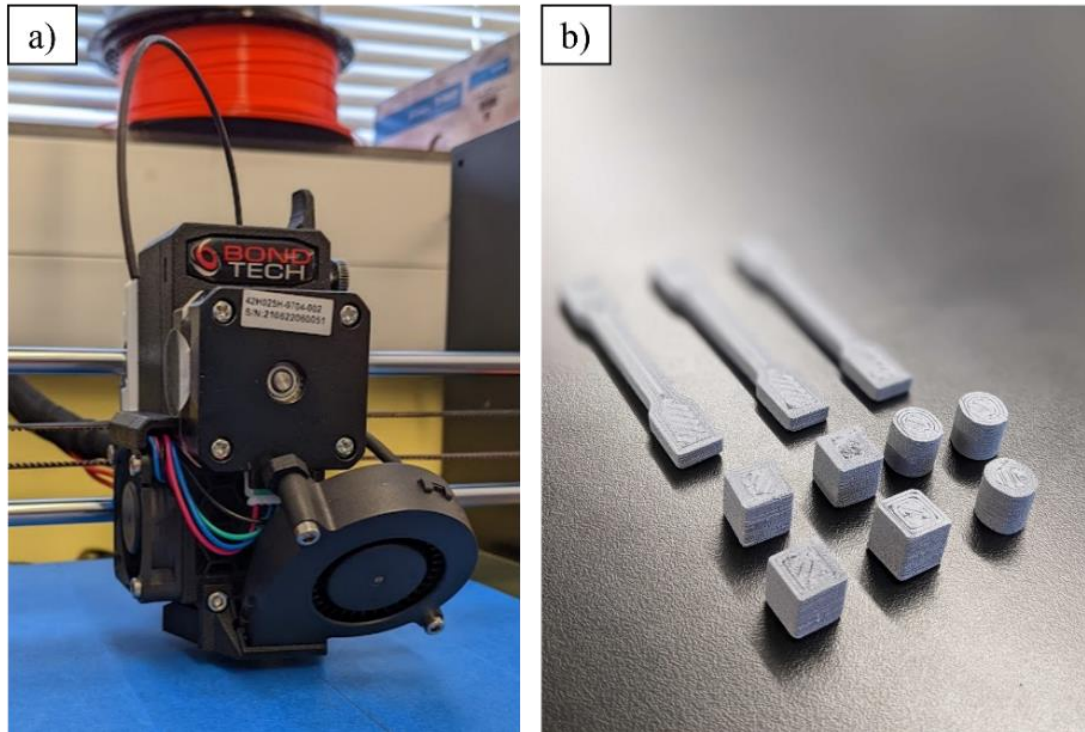


FIGURE 13 - a) 60 vol% Al-6061 filament in printer extruder, b) commonly printed parts including cubes, spheres, and sample tensile bars.

A Design of Experiments (DoE) Taguchi Analysis was conducted to correlate chosen print parameters to achieving the highest green densities. TABLE II shows the values for nozzle temperature, layer thickness, and print speed that were tested. In the series of experiments, a 0.8 mm brass nozzle was used with a 0.9 mm extrusion width. Parts with 3 perimeters, 1.0 extrusion multiplier, and 45° infill were printed. TABLE III shows the results of the initial DoE analysis, presenting the parameters that were calculated to best correlate to high green printed densities. FIGURE 14 shows the resulting Signal-to-Noise (SN) ratios that were calculated in the Minitab statistical

software to correlate the parameters to highest green density. The parameters with the highest SN ratio were the ones that correlated to the highest green density.

TABLE II

INITIAL DESIGN OF EXPERIMENTS FOR 3D PRINTING GREEN AL-6061 PARTS

Tested Parameters	Nozzle Temperature (°C)	Layer Thickness (mm)	Print Speed (mm/s)
	200	0.3	10
	210	0.35	15
	220	0.4	20
Test Number	Nozzle Temperature (°C)	Layer Thickness (mm)	Print Speed (mm/s)
1	200	0.3	10
2	200	0.35	15
3	200	0.4	20
4	210	0.3	15
5	210	0.35	20
6	210	0.4	10
7	220	0.3	20
8	220	0.35	10
9	220	0.4	15

TABLE III

INITIAL DESIGN OF EXPERIMENTS RESULTS

Test	Parameters			Density		
	Nozzle Temperature (°C)	Layer Thickness (mm)	Print Speed (mm/s)	Average Density (g/cc)	Filament Density (g/cc)	Density relative to filament (%)
Optimized Green Density	220	0.3	10	1.697	1.988	85

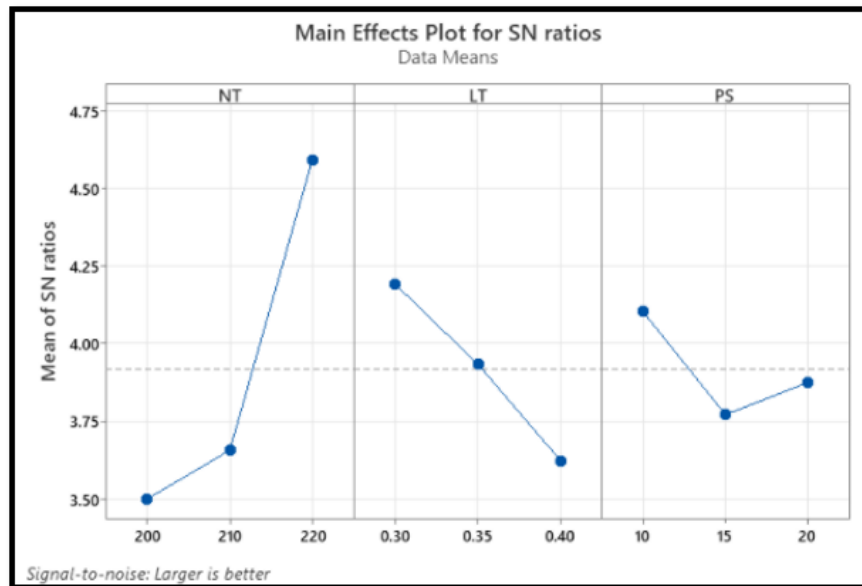


FIGURE 14 - Initial DoE Testing SN ratios

As seen in TABLE III, the chosen parameters were able to successfully print green parts that were 85% dense compared to the filament (density of 1.988 g/cc). This testing shows that the hottest nozzle temperature (220 °C), thinnest layers (0.3 mm), and slowest print speed (10 mm/s) led to the densest green parts. The selected nozzle temperature is consistent with the shear rate-dependent viscosity, shown in FIGURE 10, when the hotter of the two feedstocks (at 220 °C) featured the lower viscosity across all shear rates. Low viscosity is desired for MF³, as sufficient liquidation of the feedstock filament is achieved and better flowability occurs, allowing material to consistently deposit in each layer without clumping or clogging. The thin layer heights allow for more layers in the printed volume, prohibiting more gaps to form between the deposited beads of material. With fewer gaps between layers, more material can fill the volume and the part can be denser. The low print speed of 10 mm/s prevents defects and voids by

ensuring the material flowing through the nozzle can be more carefully deposited in each layer, as high print speeds can prevent proper material flow and even improper feature definition.

However, it is desirable to achieve as high of a green density as possible, as higher green densities can directly lead to higher sintered densities and therefore better mechanical properties after sintering (Singh, Balla, Atre, et al., 2021) (German, n.d.). Another Design of Experiments test was conducted with different settings with the goal of improving on the 85% relative green density achieved in the first DoE test. There were changes made in the second DoE test: a smaller nozzle diameter of 0.6 mm from 0.8 mm and extrusion width of 0.6 mm, the same as the nozzle diameter, from 0.9 mm, which was higher than the initial nozzle diameter. It was theorized that the parts printed in the initial DoE test did not achieve 100% relative green density due to gaps between layers in the horizontal and vertical planes, and the changes made would allow more material to fill the volume, therefore increasing the density. By decreasing the nozzle to 0.6 mm from 0.8 mm, more layers would be deposited in each horizontal-vertical cross section and allow for finer geometries to be printed. By decreasing the extrusion width to equal the nozzle diameter, more layers could be deposited in the vertical and horizontal directions, since the printer would have to print more layers to account for the “lost” material in a smaller width.

In the second DoE test, further optimization of the printing parameters (nozzle temperature, print speed, layer thickness) was examined. TABLE IV shows the printing

parameters that were tested. In this DoE test, a higher nozzle temperature of 230 °C was tested to investigate if the viscosity could be lowered to further improve material flow through the nozzle. Lower layer thicknesses 0.15 mm and 0.25 mm were added to investigate how much further the density could be increased by increasing the number of layers in the volume. The print speeds tested remained the same as the initial DoE test. TABLE V shows the results of the second DoE analysis, presenting the parameters that were calculated to best correlate to high green printed densities. FIGURE 15 shows the resulting Signal-to-Noise (SN) ratios that were calculated in the Minitab statistical software to correlate the parameters to highest green density. The parameters with the highest SN ratio were the ones that correlated to the highest green density.

TABLE IV

SECOND DESIGN OF EXPERIMENTS PARAMETERS FOR 3D PRINTING GREEN AL-6061 PARTS

Tested Parameters	Nozzle Temperature (°C)	Layer Thickness (mm)	Print Speed (mm/s)
	210	0.15	10
	220	0.25	15
	230	0.35	20
Test Number	Nozzle Temperature (°C)	Layer Thickness (mm)	Print Speed (mm/s)
1	210	0.15	10
2	210	0.25	15
3	210	0.35	20
4	220	0.15	15
5	220	0.25	20
6	220	0.35	10
7	230	0.15	20
8	230	0.25	10
9	230	0.35	15

TABLE V

REFINED DESIGN OF EXPERIMENTS RESULTS

Test	Parameters			Density		
	Nozzle Temperature (°C)	Layer Thickness (mm)	Print Speed (mm/s)	Average Density (g/cc)	Filament Density (g/cc)	Density relative to filament (%)
Optimized Green Density	210	0.25	10	1.958	1.988	99

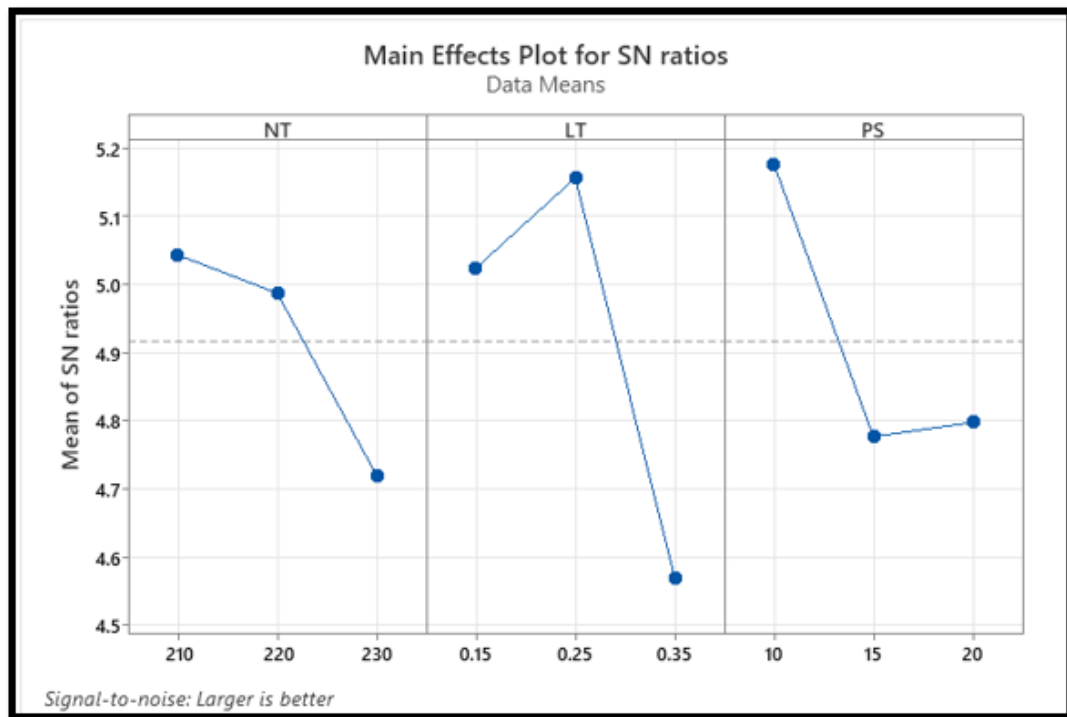


FIGURE 15 – Refined DoE Testing SN ratios

As seen in TABLE V, the second Design of Experiments test resulted in parts that were 99% dense relative to the filament, much higher than the 85% from the first DoE

test. With the smaller nozzle diameter of 0.6 mm compared to the initial 0.8 mm, more layers were able to be deposited in each horizontal-vertical cross section. The selected parameters resulting from the Taguchi Analysis in the DoE is interesting, as the lowest nozzle temperature (210 °C) was selected, whereas the hottest temperature (220 °C) was selected in the first DoE test. While 210 °C is the lowest temperature in the DoE test, it is still higher than the lowest temperature used in the initial DoE test (200 °C), so the feedstock material still has a satisfactory viscosity during printing that allows for sufficient flow through the nozzle. Shown in FIGURE 15, the SN ratio of the 220 °C nozzle temperature is not much lower than the 210 °C point, showing that both temperature values had very similar correlations to printing dense parts. Additionally, the lowest layer thickness (0.15 mm) did not feature the highest SN ratio compared to the other layer thickness values as the 0.25 mm value, in the middle between the three values, did. 0.25 mm is lower than the layer thickness selected in the initial DoE test (0.30 mm), indicating a refinement towards a more precise layer thickness that leads to higher density values in green parts. The print speed (10 mm/s) is the same as the initial DoE test, being the lowest speed tested. Overall, the second DoE test refined the printing parameters to print parts at higher green densities, due to the smaller nozzle diameter and extrusion width.

Further refinement in the final printing parameters took place in areas not analyzed in the DoE tests. TABLE VI shows relative green density values for parts printed at the settings analyzed in the second DoE test at three different extrusion multiplier values. For both DoE tests, an extrusion multiplier value of 1.0 was used. By

increasing the multiplier, the amount of material flowing through the nozzle increases, depositing more material laterally across each layer. For example, an extrusion multiplier of 1.1 will deposit 1.1x the amount of material laterally in a horizontal-vertical cross-sectional layer. The extrusion multiplier of 1.2 was used with the printing parameters selected in the second DoE test for all parts moving forward, as it led to the highest green densities compared to the other Extrusion Multiplier values.

TABLE VI
EXTRUSION MULTIPLIER EFFECT ON RELATIVE GREEN DENSITY

Extrusion Multiplier	Average Density (g/cc)	Average Relative Green Density (%)
1.0	1.68	84.38
1.1	1.79	90.28
1.2	1.96	98.44

Additionally, alternating infill angles of 0°-90° were utilized instead of the original 45° infill in further printing of green parts with the goal of reducing the gaps between layers. Further, only 1 perimeter was used instead of 3 to build more consistency between the layers in the part's infill. TABLE VII details the printing parameters used to print optimal parts based on the results of the second DoE test, described in TABLE V, the 1.2 extrusion multiplier, and the updated infill angle. FIGURE 16 shows a comparison between parts printed with the initial printing parameters outlined in TABLE III in the first DoE test (FIGURE 16a) and parts printed with the parameters shown in TABLE VII (FIGURE 16b), proving the reduction in spaces between the horizontal-vertical layers leading to the increase in green relative density.

TABLE VII

OPTIMAL PRINTING PARAMETERS USED IN PRINTING DENSE GREEN AL-6061 PARTS.

Nozzle Temperature (°C)	Print Speed (mm/s)	Layer Thickness (mm)	Bed Temperature (°C)
210	10	0.25	65
Nozzle Diameter (mm)	Extruder Multiplier	Infill Angle (°)	Number of Perimeters
0.6	1.2	0 - 90	1

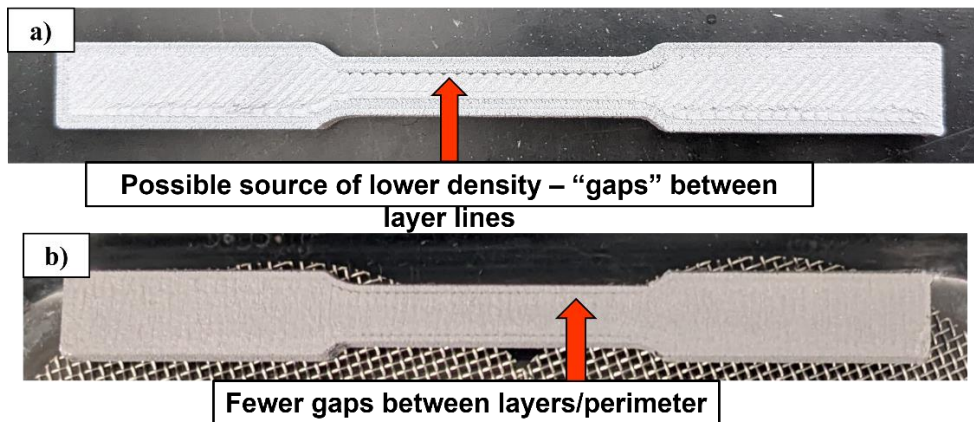


FIGURE 16 - Comparison between initial printing parameters and optimal printing parameters, reducing gaps between layers to create denser green parts

Roughness Averages (R_a) were measured on green parts printed at the conditions shown in TABLE VII to verify that the printed parts would feature smooth surfaces on the top and sides. A drawback for traditional FDM is poor surface roughness compared to other manufacturing processes, but with optimal printing parameters can come smoother surfaces. Smoother surfaces can result from more consistent extrusion of material through the nozzle, more overlap between layers from increased extrusion multipliers, finer layers with smaller nozzles, and slower printing speeds allowing for consistent material deposition (Schneidler et al., 2021). While surface roughness can certainly be a response parameter used in Design of Experiments testing to optimize printing parameters (Singh, Balla, Atre, et al., 2021), the roughness values in this study are only to quantify the smoothness of the parts printed under the selected settings and further show the smooth layer deposition resulting in dense green parts. Table VIII shows the values roughness averages across 2 surfaces on printed 10 mm x 10 mm x 5 mm green tablets printed at the ideal printing settings. When measuring along the infill layers, the roughness is much lower compared to measuring perpendicular to the infill direction. However, the small difference between the side surface roughness (7.641 μm) and top surface roughness (5.191 μm) show consistency in the smoothness of the printed parts, as it is desired that all surfaces are smooth. The higher roughness on the side surfaces results from the chosen layer thickness of 0.25 mm. If the parts were printed with lower layer thicknesses, the side roughness could be smoother. The roughness on the top surface results from the edges of each extrusion width. With the increased extrusion multiplier of 1.2, there is overlap between width edges, resulting in more material in the gaps and a smoother

surface. Additionally, the green samples measured in Table VIII were imaged under a Scanning Electron Microscope (SEM) to highlight the smoothness, shown in FIGURE 17, FIGURE 18, and FIGURE 19.

Table VIII

ROUGHNESS AVERAGES OF GREEN PARTS PRINTED WITH OPTIMAL PARAMETERS

Roughness Averages (R_a)			
Top Surface - Against Infill (μm)	Top Surface - Along Infill (μm)	Side Surface - Against Layers (μm)	Side Surface - Along Layers (μm)
7.994	5.191	13.160	7.641

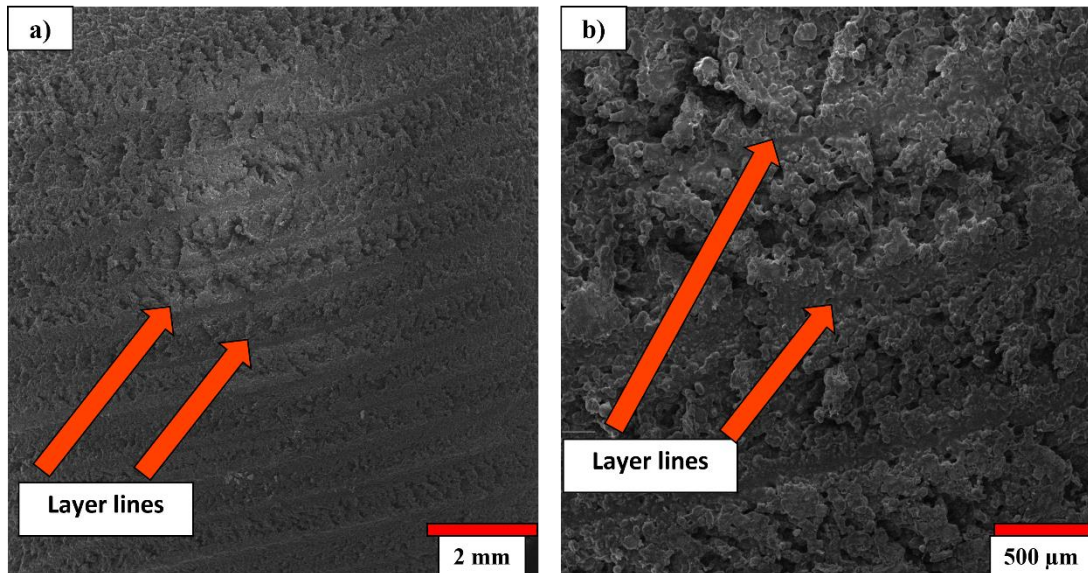


FIGURE 17 - Top surface images of printed green part, with R_a of $6.934 \mu\text{m}$ perpendicular to infill and $5.523 \mu\text{m}$ along infill

FIGURE 17a, at 29x magnification, shows the layer lines that exist on the top surface of the green parts printed with the ideal parameters. Seen in FIGURE 17b, at 100x magnification, shows that there are no gaps between the layers, allowing greater densification. FIGURE 18a, at 30x magnification, show the 0.25 mm-thick layers that are

evident on the side of the green parts with definite lines separating them. Upon closer viewing at 98x magnification in FIGURE 18b, it is clear to see that there is uniform dispersion of the metal powder-polymer binder matrix, with the polymer binder consistently coating the metal powders homogeneously, as individual metal particles are almost indistinguishable. In FIGURE 19a, imaged at 29x magnification, a green sample was cut to expose the cross section of the inside surface between layers. No distinction between the 0.25 mm-thick layers can be seen, revealing a smooth and homogeneous part. Any inconsistencies result from chunks breaking or becoming uneven during cutting. FIGURE 19b, imaged at 98x magnification, further reveals the homogeneity of the metal powder-polymer binder matrix, with individual particles not being distinguishable.

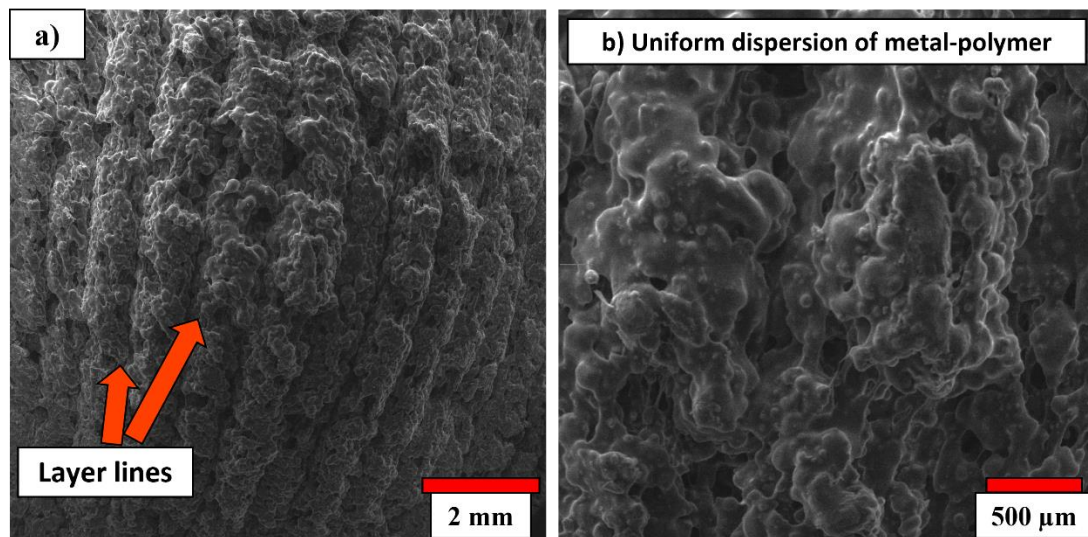


FIGURE 18 - Side surface images of printed green part, with Ra of 11.410 μm perpendicular to infill and 5.840 μm along infill

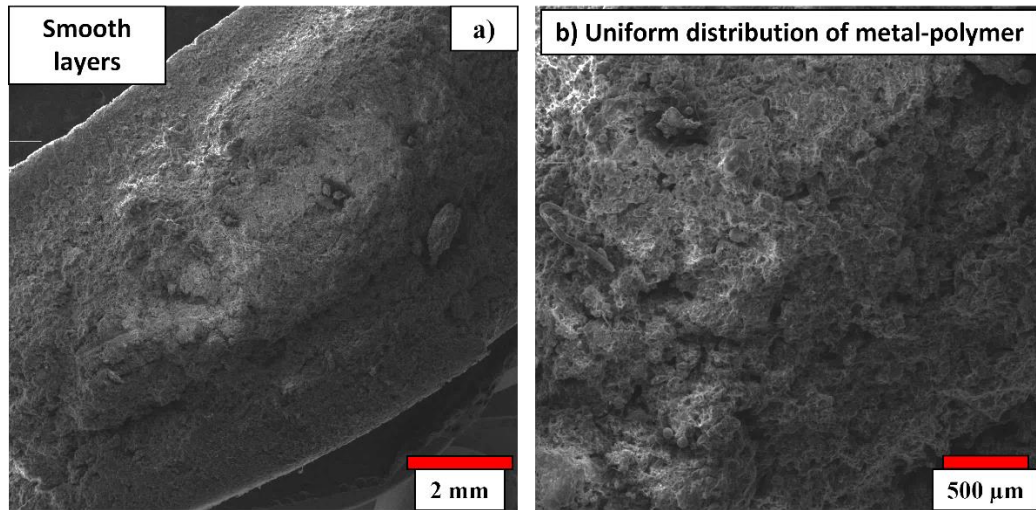


FIGURE 19 - Cross section images of printed green part

This paper demonstrates successful production of Al-6061 metal alloy powder-polymer binder feedstocks and printing of green parts from filaments. Design of Experiments Taguchi Analyses optimize the results of printing with the Al-6061 feedstock filament, producing dense green parts ready for successful debinding and sintering. The quality of the printed parts is also validated with surface roughness measurements and SEM images, proving material homogeneity and consistency between printed layers.

2.3 THERMAL STATE EXPERIMENTAL METHODS

Green printed parts were run through a two-step solvent and thermal debinding procedure before sintering to remove the binder components. The green parts were solvent debound in n-heptane solution at 64 °C for 8 hours. The resulting “brown” parts

were set in an oven (Blue M, New Columbia, PA) overnight at 48 °C to remove the remaining solvent and be completely dry before the thermal debinding process.

Before a thermal debinding profile was developed and implemented, metal powder-polymer binder feedstock samples were thermally degraded via a thermogravimetric analyzer (TGA, SDT Q600, TA Instruments, New Castle, DE, USA). The thermogravimetric analysis (TGA) tests were conducted in a nitrogen (N₂) atmosphere, heating the feedstock samples at 3 °C/min up to 600 °C. The thermal debinding of the printed parts was also done in a nitrogen furnace atmosphere (CM Furnaces Inc., Bloomfield, NJ, USA) at 40 ft³/hour, heating at 1 °C/min and holding at 280 °C, 330 °C, and 450 °C for 4, 3, and 4 hours, respectively, for complete binder removal. In the same furnace, the sintering temperature for thermally debound parts was chosen to be 625 °C, with the heating rate of 3 °C/minute, and a hold time at the sintering temperature being 2.5 hours. This sintering temperature point falls well below the melting point of aluminum and was derived from previous studies involving sintering aluminum compacts with similar powder characteristics and from the powder manufacturer indications (Schaffer & Hall, n.d.), (Wu et al., 2021), (Liu et al., 2007), (Schaffer et al., 2006).

2.4 THERMAL STATE RESULTS AND DISCUSSION

To remove all the polymer binder components, the green printed parts were taken through a two-step solvent and debinding process. In the solvent debinding process, 40% of the polymer binder, corresponding to approximately 8% of the weight of the total green part, is dissolved. A portion of the backbone, plasticizing, and elastomer phases of the polymer binder are dissolved in this step before thermal debinding. These dissolved polymers act as “sacrificial” polymers that open channels throughout the part that allow the rest of the polymer binder to have a means of escaping during thermal debinding. To determine the ideal time of solvent debinding in the n-heptane solution, parts were solvent debound at 4, 6, and 8 hours. The part mass was measured before and after the solvent debinding to compare the amount of mass that was lost. Shown in TABLE IX, the 8-hour debinding time was chosen as it indicated that the appropriate amount of the polymer binder was dissolved, leaving around 92% of the part’s mass remaining and indicating that close to 40% of the polymer binder weight was dissolved as desired.

TABLE IX
SOLVENT DEBINDING RESULTS

Test Length (hour)	Average Binder Weight Loss (%)	Average Total Part Mass Remaining (%)
4	29.32	94.21
6	34.71	93.79
8	38.73	92.68

To develop the thermal debinding profile, thermogravimetric analysis (TGA) tests were conducted on the metal powder-polymer binder feedstock. FIGURE 20 shows the results from a standard TGA test. The left vertical axis represents the total weight (%) of the feedstock sample while the right axis represents the rate that the weight of the feedstock sample was degraded.

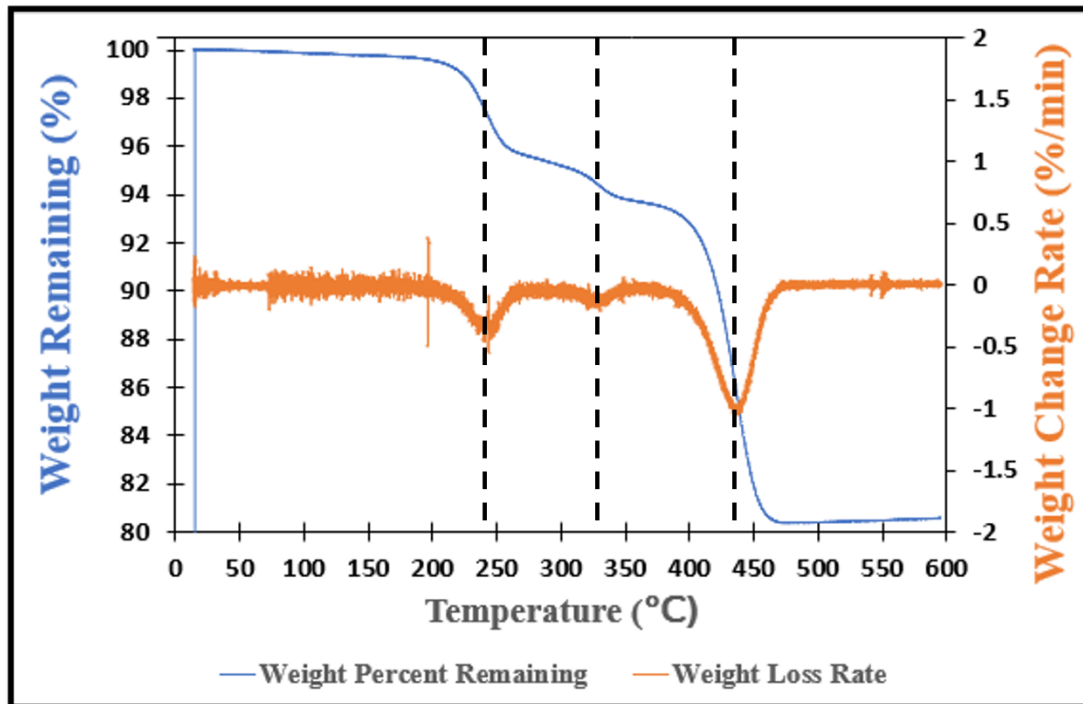


FIGURE 20 - TGA results of feedstock to understand the thermal debinding cycle.

As can be seen in FIGURE 20, the weight of the sample ends at around 80.5 % of the initial weight before the cycle. In this test, the feedstock consisted of 60 vol% of Al-6061 metal powder, corresponding to 80.3 % by weight. This test proves that the feedstock sample was filled with the appropriate amount of powder and that the full feedstock batch remained homogeneous during mixing, consisting of the appropriate amount of metal powder and polymer binder in each segment of the feedstock.

The points where the weight loss rate greatly decreased were also noted from FIGURE 20. The three “dips” in the rate correspond to temperatures near 240 °C, 330 °C, and 440 °C, indicating the points where maximum binder removal was reached. Based on these decomposition points, debinding temperatures of 280 °C, 330 °C, and 450°C were

selected, with the maximum and minimum temperatures being increased to allow for greater binder removal.

Hold times at those temperatures of 5, 4, and 6 hours were selected at the 280 °C, 330 °C, and 450 °C, respectively, to ensure that all the organic compounds were eliminated at each step, as sintered parts would have greater masses than the TGA feedstock samples and therefore contain greater amounts of the binder that would need to be burned during a thermal debinding cycle. It is essential that all the polymer binder system is removed during thermal debinding to allow for minimal chemical reaction during sintering, reduced slumping of the sintered parts and prevention of organic residue in the pores that can affect sintered porosity (German & Metal Powder Industries Federation., 2011). Therefore, the increased temperatures and hold times are necessary to ensure that all the polymer binder is removed before the sintering cycle begins. A heating rate of 1 °C/minute was selected in the thermal debinding cycle to allow for maximum time for the polymers to be degraded before entering the sintering cycle in higher temperatures.

In addition to the TGA test conducted on the feedstock, a sample of the Al-6061 metal powder was tested. In this test, the powder sample was heated in an air atmosphere at 3 °C/minute to 600 °C. Oxidation is a common occurrence in sintering aluminum powder (Fang, 2010) and it was desired to observe the phenomenon before initial sintering tests began. When oxidation occurs in metal powders, a surface oxide layer forms as a result of the relative diffusion rates through the metal and oxide, preventing effective sintering (Lumley et al., 1999). Oxidation can occur in Al-6061 powders at

heat-treatment temperatures as low as 230 °C (Ernst et al., 2020), so investigating the possibility of oxidation in the received Al-6061 powder was important. As seen in FIGURE 21, the test results make use of the same axes as the TGA test shown in FIGURE 20, with the left vertical axis representing the total weight (%) of the powder sample and the right axis representing the rate that the weight of the sample changed. At around 350 °C, there is an increase in the weight of the powder sample, increasing to 100.4 % weight by the end of the test. This is most likely an indication of oxidation, highlighting the possibility that the powders can oxidize in future sintering cycles when air atmospheres are used, and the sintering cycle is not designed properly.

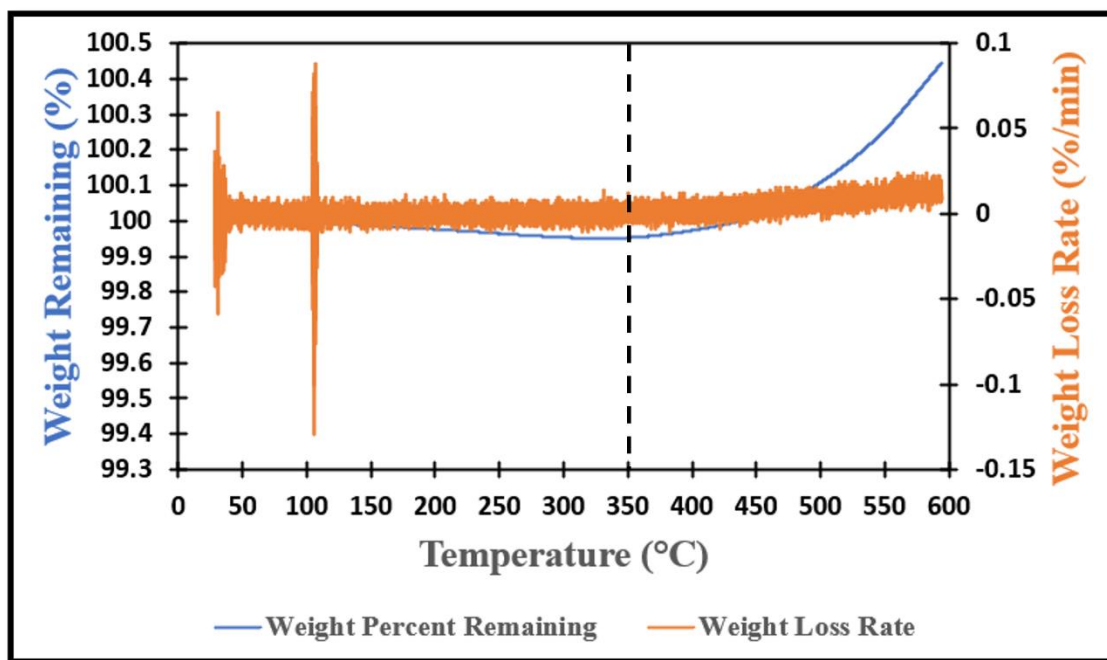


FIGURE 21 - TGA results of pure Al-6061 powder

Based on the TGA data shown in FIGURE 20 and review of the open literature on sintering aluminum powder, a combined thermal debinding-sintering thermal cycle was

developed and is shown by a temperature versus time plot in FIGURE 22. This cycle makes use of the temperature hold times of 5, 4, and 6 hours at the 280 °C, 330 °C, and 450 °C, temperature points, respectively. The heating rate for thermal debinding was of 1 °C/minute. A sintering temperature of 625 °C for 2.5 hours was selected with a heating rate of 3 °/minute after the thermal debinding portion. The thermal cycle was conducted in a box furnace with a nitrogen atmosphere flow rate of 40 ft³/hr. Results of the sintering of the printed Al-6061 parts is discussed in CHAPTER III. SINTERING OF AL-6061 PRINTED PARTS

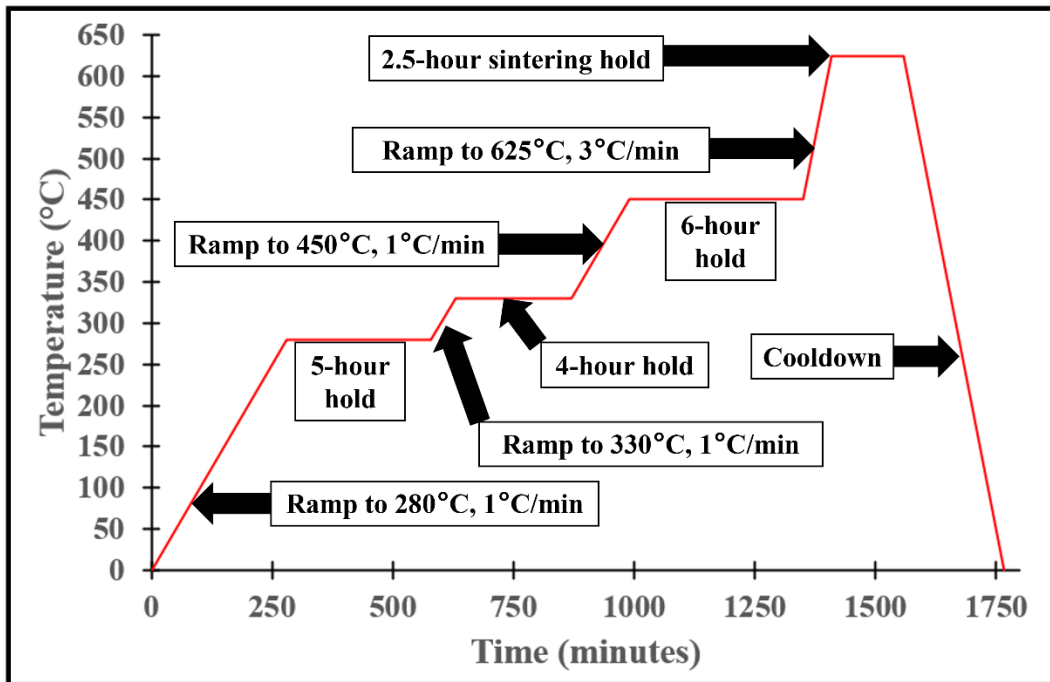


FIGURE 22 - Thermal debinding-sintering thermal cycle of solvent debound printed Al-6061 parts

2.5 CONCLUSIONS

This work analyzed the Metal Fused Filament Fabrication (MF³) manufacturing process applied to an aluminum-6061 alloy metal powder-polymer binder feedstock filament. Powder characterization was performed to better understand the powder's packing ability, density, and particle shape. Metal powder-polymer binder feedstocks at various solids loading amounts were produced and a solids loading of 60 vol% was chosen. Viscosity measurements of 60 vol% feedstocks were conducted to build an understanding of the material's printability and homogeneity. Two Design of Experiments Taguchi Analysis tests were performed to determine the optimal printing parameters for printing with the feedstock filament and producing dense green parts. An appropriate solvent debinding cycle was determined to dissolve the correct amount of the polymer binder before thermal debinding. Based on thermogravimetric analysis (TGA) data, a thermal debind profile was designed with the goal of degrading all the polymer binder before sintering. Based on literature review, a complete thermal debinding-sintering cycle was designed with the goal of producing Al-6061 comparable to those produced by MIM. The MF³ process is a topic of great study, and this work further validates its applicability and effectiveness with a new metal alloy.

CHAPTER III. SINTERING OF AL-6061 PRINTED PARTS

3.1 INTRODUCTION

In this work, many sintering tests on printed Al-6061 parts via a metal powder-polymer binder feedstock filament system are conducted with the goal of producing full densities comparable to parts produced via Metal Injection Molding (MIM). Many challenges exist in sintering aluminum powder compacts, especially in the Metal Fused Filament Fabrication (MF³) manufacturing process, which utilizes a two-step solvent and thermal debinding process to dissolve and burn the polymer binder system from the printed part before sintering. Parameters used in the thermal cycle to fully debind and sinter the printed Al-6061 parts are studied and adjusted at each test to optimize the cycle performance. Parameters studied in this work include gas flow rate, sintering temperature, thermal debinding temperatures and hold times, and sintering hold time. Factors that influenced adjustment of parameters at each sintering test included presence of pores/voids in polished parts, sintered density, hardness, and surface oxidation.

In the open literature, much work has been conducted on optimizing sintering cycle parameters to produce metal parts with comparable mechanical properties and densities. In a study by Lue et al., the effect of sintering temperature hold time on the resulting density, resistivity, and Vickers hardness of $\text{Ti}_3\text{SiC}_2/\text{Cu}$ composite samples were studied. It was found that by increasing the sintering temperature, the density increased while the resistance and Vickers hardness decreased, providing a potential solution for increasing sintered density in the printed Al-6061 parts (Lu et al., 2012). In another study, process conditions such as sintering times, sintering temperatures, and presence of graphene additive were adjusted in many tests of sintering an aluminum alloy composite to see the effects on the apparent density and hardness. The sintering process conditions that correlated to higher densities and hardness were then chosen to design an optimized thermal cycle (Gürbüz et al., 2018). Additionally, one study utilized the Taguchi method of Design of Experiments when analyzing the microstructure and mechanical properties of sintered Al-7055 parts. Therefore, a thermal cycle with an optimized sintering temperature of 560 °C, hold time of 150 minutes, and pressure of 12 MPa was derived (Wang et al., 2021). In a similar study, Al-6061 powder compacts were sintered across three tests in a Design of Experiments Taguchi method involving the die compaction pressure, sintering temperature, sintering hold time, and heating rate parameters. The microstructure, densities, and mechanical properties were analyzed to determine the optimal sintering conditions (Arockiasamy et al., 2011). Making use of the MF³ manufacturing process with an aluminum-7075 alloy powder-polymer binder filament, another study optimized the sintering heating rate (30 °C/min) and argon pressure to

increase the density of the sintering parts, achieving 2.72 g/cm³ (Ding et al., 2022). These studies show techniques used to optimize thermal processing conditions that carry great effects in the performance of designed sintering cycles. Similar techniques are used in this work to conduct initial thermal debinding and sintering experiments on solvent debound Al-6061 parts printed from the metal powder-polymer binder feedstock filament.

3.2 EXPERIMENTAL METHODS

The thermal debinding and sintering of the printed parts was done in a nitrogen furnace atmosphere (CM Furnaces Inc., Bloomfield, NJ, USA). Sintered parts were polished with 320, 400, 600, and 800 – grit silicon carbide paper. Resulting densities of the sintered parts, ρ , were measured using the Archimedes method with a density determination kit (Mettler-Toledo AG Laboratory & Weighing Technologies, CH-8606 Greifensee, Switzerland) using

$$\rho = \frac{A}{A-B}(\rho_o - \rho_L) + \rho_L \quad (1)$$

where A is the weight of the sample in air, B is the weight of the sample in an auxiliary liquid such as ethanol, ρ_L is the density of air (0.0012 g/cm³), and ρ_o is the density of the auxiliary liquid. Vickers Hardness (HV) was measured for each sample in each sintering

run via a M-400 Microhardness Tester (LECO Corporation, St. Joseph, MI). The hardness values were calculated from the measurements using

$$HV = \frac{1.8544 F}{d^2} \quad (2)$$

where F is force applied by the indenter (kgf) and d is the average width of the diagonal left by the indenter (mm).

3.3 SINTERING RESULTS/DISCUSSION

Before conducting sintering tests on the parts printed from the Al-6061 metal powder-polymer binder feedstock filament, samples of the pure Al-6061 powder were sintered. In the first test with the pure powder, an air atmosphere was used instead of nitrogen, and the sample was heated to 625 °C at 5 °C/min and holding for 2 hours. As a result of using an air atmosphere, oxidation was observed on the top surface of the powder compact, shown in FIGURE 23. Insufficient flow of the proper atmosphere leads to insufficient sintering, which also can cause cracking and loose powder residue that is not sintered in the compact, and these results are also shown in FIGURE 23. However, when using the nitrogen atmosphere, improved sintering results of similar powder samples were seen. After polishing the top surface of the sintered compacts, the samples' densities were measured, averaging to be 87.17 % relative to that of the pycnometer

density of the Al-6061 powder (2.71 g/cm^3), shown in TABLE I. As a starting point for initial sintering experiments, this is a suitable density for the pure powder samples, and the sintering cycle used in these tests was applied to initial sintering cycles with the printed parts. In initial sintering experiments conducted on the aluminum-6061 alloy powder by Kymera International, the supplier of the powders used in this work, 99% relative theoretical density was achieved, showing the potential that exists for sintering this alloy. The polished sample resembles standard Al-6061 material with the reflective surface and density. After sintering and before polishing, the top layer has a powdered texture and slight discoloration. After polishing, it is proven that most of the powder particles are indeed sintering during the thermal cycle, forming near-dense compacts, and building confidence in the chosen thermal cycle. Vickers Hardness of a polished sample was measured to be 154 HV, also reported in TABLE XIII. FIGURE 23 shows the progression of the successful sintering tests with loose powder as well as the test that utilized the air atmosphere, where oxidation and cracking were observed. It was important to conduct initial testing on the loose powder samples before the printed parts to observe the challenges of oxidation and insufficient sintering and validate the sintering cycle with the chosen atmosphere.

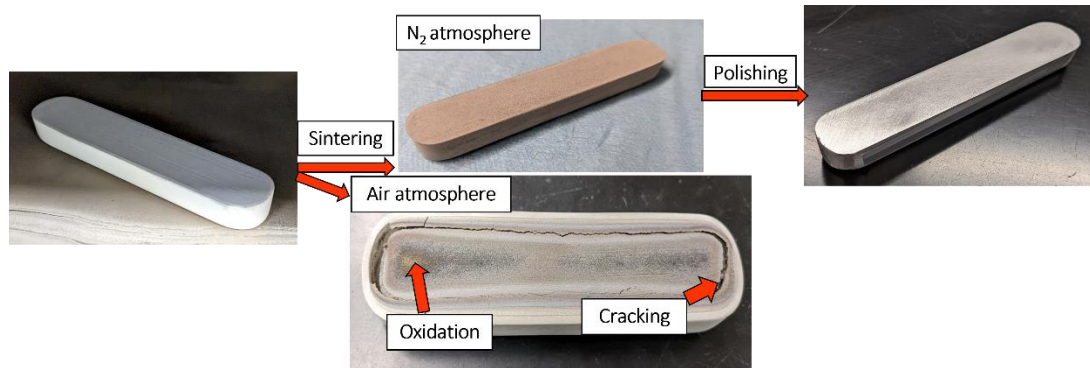


FIGURE 23 - Progression of sintering and polishing pure Al-6061 powder samples

In the present work, 4 sintering runs were conducted on printed Al-6061 powder-polymer feedstock filament samples. After evaluating the results of each test, parameters such as the thermal debinding temperatures, hold times, and gas flow rates were adjusted with the goal of improving the results. FIGURE 24 showcases some of the challenges encountered in initial runs that caused parameters to be adjusted. TABLE X describes the parameters and results seen in each of the sintering runs. Vickers hardness of one sample from each run was measured and relative densities of most of the parts were measured using the Archimedes principle.

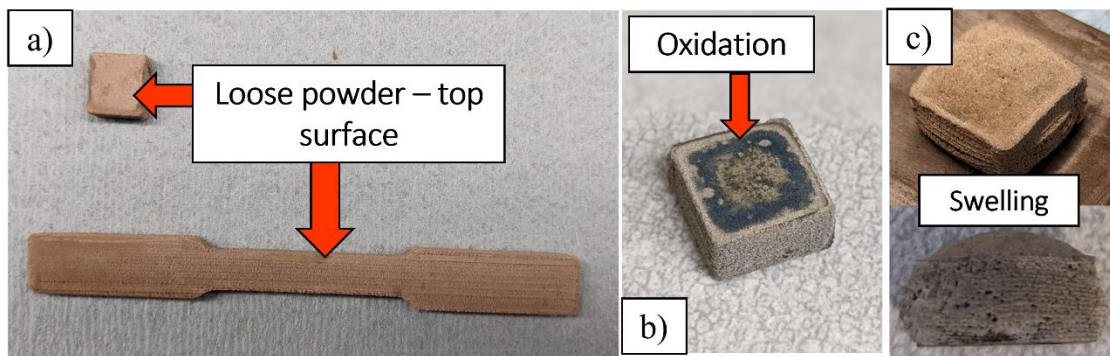


FIGURE 24 - Challenges encountered in initial sintering cycles, including loose powder residue, oxidation, and swelling

TABLE X
SINTERING RUN PARAMETERS AND RESULTS

Run	1	2	3	4
Thermal Debind Hold Points (°C)	250, 350, 475	280, 330, 450		
Thermal Debind Hold Lengths (hrs)	2, 1.5, 3	5, 4, 6		
Sintering Temperature (°C)	625			
Sintering Hold Length (hrs)	2		2.5	
Gas Atmosphere	Nitrogen			
Gas Flow rate (ft³/hr)	20			40
Relative Sintered Density (%)	70.69	71.65	72.38	71.65
Vicker's Hardness HV	181	150	107	135
Shrinkage (%)	-			3.47

In the initial runs, the parts were not sintered sufficiently, as most parts featured a layer of loose powder on the top surfaces, pictured in FIGURE 24a. As the sintering cycle progressed, the powder layers on the printed parts were greatly reduced, indicating that greater sintering was occurring. By Run 4, there was almost no loose powder on the top surface of the parts. Another challenge with sintering aluminum is oxidation, as aluminum oxide (Al_2O_3) forms a thin layer on the outside of the compact that causes an increase in the total weight and makes the material more difficult to sinter (Schaffer & Hall, n.d.). FIGURE 24b shows an example of oxidation on the bottom surface of a printed part that was touching the setting plate. This oxidation occurrence was only on surfaces touching the setting plates and was almost non-existent by Run 4, with the entirety of the parts having little to no discoloration.

One of the main goals of running the printed parts through a thermal debinding-sintering cycle is to completely degrade the polymer binder system from the part, leaving only the elemental metal alloy. FIGURE 24c shows a part that did not experience solvent debinding before being cycled through Run 3. This part shows the significant swelling that can occur if there is insufficient binder burnout during the thermal cycle. When this occurs, the polymer escapes the part volume later in the cycle, before or during sintering of the metal powder particles, causing the distortion. The warping that is shown on the side and top surfaces was common in many parts through Runs 1-3, when all the other parts sintered had been through an 8-hour solvent debind cycle prior to the thermal cycle. To further improve the binder degradation in the thermal debinding portion of the cycle, the amount of time holding at each temperature hold point was increased. After Run 1, the times were doubled with an extra hour added on. Once the change was made, swelling did decrease, but did not fully go away until after Run 4, where the parts experienced no distortion. The thermal debinding temperatures were adjusted after Run 1 to resemble the thermogravimetric analysis (TGA) profile of the feedstock more closely, as Run 1's temperatures were slightly higher. The goal of the adjustments was to avoid over-burning the part while better resembling the TGA profile. These temperature adjustments were relatively minor (differing by at most 30 °C) and did not have a great effect on the binder degradation. Therefore, increasing the thermal debind hold times assisted in degrading the polymer binder from the printed part.

The sintering hold time was increased from 2 to 2.5 hours after Cycle 2 to increase the sintering density. Sintering was occurring in the parts, but voids were still

present after polishing. While the density did increase to 72.03% relative to the pycnometer density of the Al-6061 powder (2.71 g/cm^3) by Run 3, it was not a large improvement from previous runs. In Runs 1 and 2, only 1 and 2 samples were measured, respectively. In Runs 3 and 4, 6 and 4 samples were measured, respectively. Another parameter that was adjusted was the nitrogen gas flow rate, increasing from $20 \text{ ft}^3/\text{hr}$ in Runs 1-3 to $40 \text{ ft}^3/\text{hr}$ in Run 4. The presence of a nitrogen atmosphere is essential to reducing porosity in sintered aluminum compacts (Schaffer et al., 2006). By increasing the flow rate, the goal was to reduce the porosity and increase the sintered density, but as shown in TABLE X and TABLE XI, the density did not increase greatly. TABLE XI shows the density data for each part in Runs 3 and 4, showing that even as part geometries differed, the densities were consistent, as the standard deviation was lower than 2%. To compare this work's sintered density values, in one study by Schaffer et al., 94% relative sintered density was reported for aluminum-6061 alloy (Schaffer et al., 2001). In another study by Wu et al., density of 2.732 g/cm^3 (over 100% relative density of Al-6061 powder) of 2024Al alloy was achieved (Wu et al., 2021). In initial aluminum-6061 sintering tests conducted by Kymera International, the supplier of the powder used in this work, 99% relative density was achieved (Kymera International, Durham, North Carolina). While the average sintered values are low compared to other aluminum sintering studies, this does provide a good starting point for future tests to improve upon.

TABLE XI
DENSITY MEASUREMENTS FOR RUNS 3 AND 4

Run 3			
Part	Density (g/cc)	Relative Density (%)	Geometry
1	1.99	73.16	10mm x 10mm x 5mm
2	1.98	72.80	
3	1.90	70.15	
Average	1.96	72.03	
4	1.90	70.02	20mm x 20mm x 5mm
5	2.04	75.21	
6	1.98	72.97	
Average	1.97	72.73	
Total Average	1.96	72.38	-
Standard Deviation	0.05	1.98	-
Run 4			
Part	Density (g/cc)	Relative Density (%)	Size
1	1.96	72.14	10mm x 10mm x 5mm
2	1.93	71.13	
Average	1.94	71.63	
3	1.99	73.34	20mm x 20mm x 5mm
4	1.90	70.00	
Average	1.95	71.67	
Total Average	1.94	71.65	-
Standard Deviation	0.04	1.42	-

While the initial sintering density data does not indicate sufficient sintering, there are indications that sintering is still occurring. After each cycle, the parts all retained a thin layer of powder buildup that was easily polished. This powder was not loose but did contain a rough surface texture. After polishing, a smooth finish resembling standard

aluminum parts was revealed. Many voids still existed throughout the part, but it was mostly seen that sintering was occurring, forming an almost fully dense compact.

FIGURE 25 shows 2 samples from Run 4 before and after polishing, revealing the sintering behavior that was taking place during a thermal cycle. The present voids have a much rougher texture similar to the top surface, indicating that these are areas where the powder particles were heated but full sintering did not occur. However, these surface finishes build confidence that the initial sintering runs are successful, and that full density is achievable as the porosity decreases.

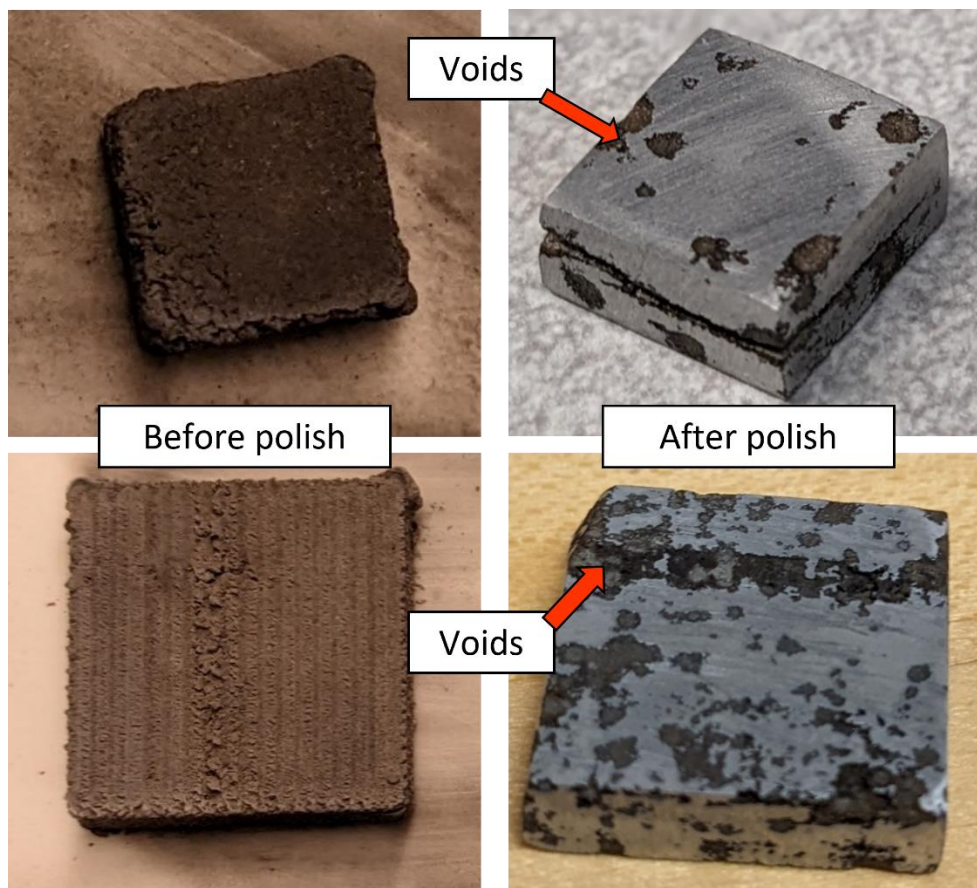


FIGURE 25 - Run 4 sintered samples before and after polishing

Shrinkage was measured in all of the parts in Run 4, averaging to be 3.47% in all directions, as shown in TABLE X and TABLE XII, where each part's shrinkage is shown. Shrinkage was not measured in Runs 1-3, as it was observed that there was negligible dimensional variance after sintering. Over 2% shrinkage during sintering with an aluminum alloy with 1.5 % by weight of Mg was observed in one study by Schaffer et al., showing that sufficient sintering can occur with low shrinkage (Schaffer et al., 2001). In initial sintering experiments with the aluminum-6061 alloy powder conducted by Kymera International, the supplier of powders used in this work, 10.7% shrinkage was observed when 98% relative sintered density was achieved. With the aluminum-6061 alloy powder, greater shrinkage may occur with improved sintering densification. While the amount of shrinkage seems to be low, indicating insufficient sintering, it is comparable to some aluminum sintering studies and does show that sintering between the aluminum powder particles is starting to occur (German, n.d.).

TABLE XII
SHRINKAGE DATA FOR RUN 4

Part	Shrinkage (%)	Original Dimensions (mm)
1	3.7	10 x 10 x 5
2	3.77	
3	3.37	20 x 20 x 5
4	3.04	
Average	3.47	
Standard Deviation	0.34	-

Vicker's Hardness (HV) testing was conducted on one sample from each of the 5 runs. The measured hardness values are show in TABLE XIII and are compared to the

standard hardness value of Al-6061 alloy, 107 HV (ASM Material Data Sheet, n.d.). Overall, the tested specimens were higher than the standard value, being at most 44% higher. However, Run 3 saw an average value being exactly the same as the standard, and Run 4 was only 26% different, showing that the results improved as the runs progressed. The Standard Deviation across all 4 runs was low, coming out to be 19, showing that none of the tests differed too greatly from the standard value. A sample from the initial loose powder sintering run under nitrogen atmosphere was also included, differing from the standard as much as Run 1 (44 %).

TABLE XIII
HARDNESS RESULTS FROM EACH SINTERING RUN

Standard HV	Run	Average HV	Difference from Standard (%)	Standard Deviation
107	Pure Powder	154	44	29
	1	181	44	37
	2	150	41	41
	3	107	0	17
	4	135	26	31
	Total		145	36

In addition to the sintering tests conducted at the University of Louisville, Kymera International (Velden, Germany), the supplier of the Al-6061 metal powder, conducted sintering tests on printed specimens. 8 total parts were tested under two different thermal debinding conditions. 4 parts were thermally debound at 500 °C for 1 hour, with 2 of the parts experiencing no prior debinding and the other 2 being solvent debound beforehand. 4 other parts were thermally debound at 500 °C for 4 hours, with 2

of the parts experiencing no prior debinding and the other 2 being solvent debound beforehand. All of the parts were sintered at 625 °C for 2 hours after heating at 2 °C/min. The shrinkage, mass change, and sintered density data for the parts are shown in TABLE XIV.

TABLE XIV
KYMERA SINTERING DATA

Debinding Time (hr)	Debinding Status	Relative Green Density (%)	Shrinkage (%)	Mass Change (%)	Relative Sintered Density (%)
1	non debinded	90%	1,9	-18,6	47%
	partially debinded	88%	-6,2	-11,6	64%
4	non debinded	74%	-2,7	-18,1	47%
	partially debinded	85%	-8,7	-11,7	70%

With the maximum relative sintered density reaching 70% that of the pure powder density, the initial data is comparable to the sintering runs conducted at the University of Louisville, as the highest relative sintered density was reported to be 72.38%, shown in TABLE X. Parts that were solvent debound prior to sintering experienced higher relative

sintered densities (64% and 70%) compared to those that were not solvent debound (47%). The shrinkage rates were higher than the shrinkage measured at the University of Louisville (3.47% in TABLE X), as the parts that were solvent debound before sintering experienced 6.2% and 11.7% shrinkage. The parts that were solvent debound and thermally debound for the longer time (4 hours) experienced the greatest shrinkage (11.7%) and saw the greatest relative sintered density, showing that more sufficient sintering was occurring due to the more complete binder degradation. The greater sintering results in the parts with more complete binder degradation is also seen in FIGURE 26, where microstructures of parts that were solvent debound prior to sintering and parts that were not as imaged. As can be seen, there is much greater porosity in the parts not solvent debound than the parts that were.

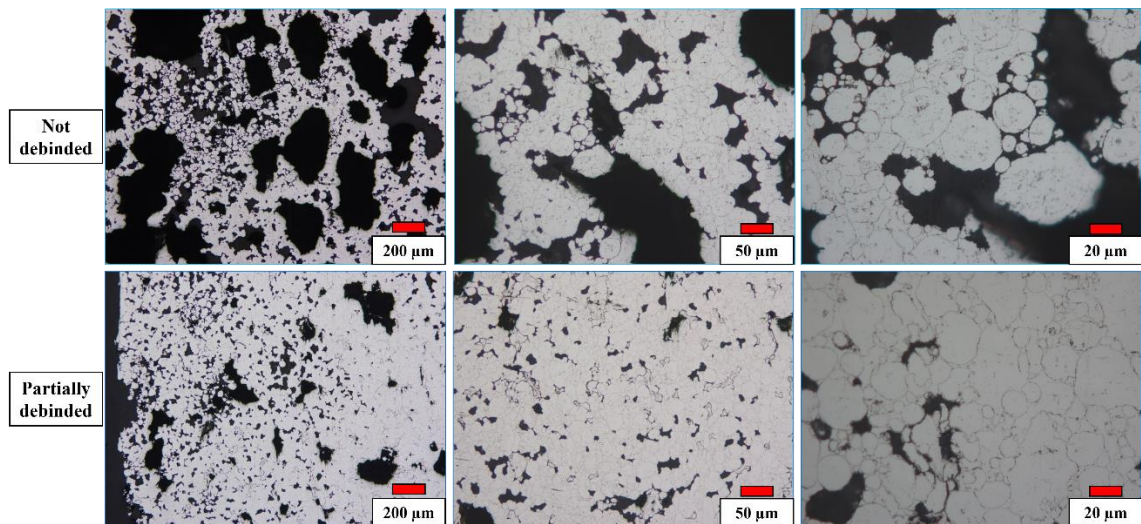


FIGURE 26 - Kymera sintering tests microstructure images

While these tests do feature great porosity and low sintering densification, there are many insights to be gained. The tests prove the importance of the solvent debinding

procedure for the particular binder system, as parts that were not satisfactorily debound experienced worse sintering results. In future sintering tests, completely degrading the binder system will be the greatest priority in improving the sintering results of the printed Al-6061 parts.

2.5 CONCLUSIONS

Although there are a great number of challenges present in sintering aluminum, they are highlighted and improved upon by the initial runs described in TABLE X. These insights allow for further optimization of the thermal cycle that can be verified with more testing. The goal of producing high-quality sintered Al-6061 3D printed geometries can be further realized with mechanical property and microstructure characterization of future sintered parts.

CHAPTER IV. CONCLUSIONS/FUTURE WORK

This work successfully demonstrates the MF³ process with aluminum-6061 alloy. Metal powder-polymer binder feedstocks were produced at 60 vol% of the Al-6061 powder (≈ 80 % by weight) and used to create flexible, spool-able filaments. These filaments were able to be used in a traditional FDM 3D printer to produce green parts at 99% density relative to the filament, minimizing voids and defects. Complex, detailed geometries were successfully printed with the chosen printing settings. Based on TGA data, the printed parts were run through a two-step solvent and thermal debinding process before sintering. Many sintering runs were conducted that highlighted the challenges experienced when sintering aluminum powder. While full densification was not realized, a framework was established for future experimentation. These results demonstrate the capability of the MF³ process in its application with the aluminum-6061 alloy, successfully fabricating complex three-dimensional parts that will be comparable to those parts fabricated via MIM.

Further optimization of the steps in the demonstrated MF³ process is certainly possible. Further refinement of the sintering cycle is needed to fully sinter the printed parts and reach higher densities. Variables in the chosen sintering cycle may be changed to optimize the cycle used in current tests. A Design of Experiments Taguchi Analysis, conducted in this work on the printing parameters used in printing green parts, can be utilized to determine the most ideal combination of thermal cycle parameters to lead to denser parts. Once high sintered densities are reached in the printed parts, mechanical properties can be investigated. Tensile testing, microstructure imaging, and impact testing can be conducted to compare the final parts to other Al-6061 parts made in other manufacturing methods and ensure minimum porosity, defects, and oxidation. Additionally, filaments in this work were produced at 60 vol% of the Al-6061 powder (\approx 80 % by weight), but more filaments can be fabricated at different solids loadings, investigating the effects of the amount of metal powder in the powder-polymer matrix on printability, sintering results, and mechanical properties. Finally, greater printing of green Al-6061 parts can occur, making use of generative design and topology optimization design methods to utilize thin structures and cellular lattice features. By printing structures designed with these techniques, the MF³ process with this metal can be further validated in fabricating more complex geometries with light-weighting features and optimized mechanical performances.

APPENDIX I. MF³ OF 17-4 PH STAINLESS STEEL

In this work, the Metal Fused Filament Fabrication (MF³) process was validated using a 17-4 PH Stainless Steel filament purchased from an outside vendor (Matterhackers, Lake Forest, CA, USA). The filament featured a diameter of 1.75 mm and a proprietary polymer binder system with the stainless-steel powders making up the filament. Once green parts were printed, they were shipped to another outside vendor for debinding and sintering (DSH Technologies, LLC, Cedar Grove, New Jersey, USA). Parts that would traditionally be machined by a partnered machine shop (Monticello Tool & Die, Monticello, KY, USA) were printed, including a helical gear. Other parts that were used to measure mechanical properties, density, and shrinkage were also printed, including 10 mm x 10 mm tablets and tensile bars (ASTM E8 standard). Pictures of the sintered parts are shown in FIGURE 27.

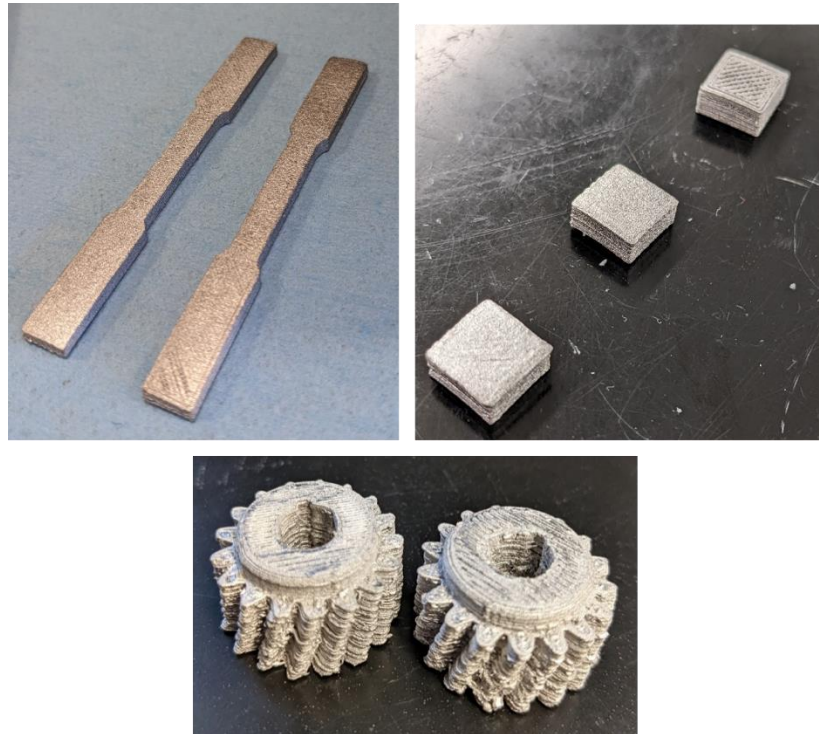


FIGURE 27 - Sintered parts printed with 17-4 PH stainless-steel filament

Final printing parameters of the 17-4 PH stainless-steel parts include a 250 °C nozzle temperature, 15 mm/s print speed, 0.25 mm layer thickness, 0.6 mm extrusion width with a 0.6-mm diameter hardened steel nozzle, 0-90 ° infill, 120 °C bed temperature, and 1.1 Extrusion Multiplier. The average sintered density of parts printed at these settings was 7.17 g/cm³. More work on refining the printing settings to achieve higher green density can be done. There was an average shrinkage of 21.1% across all directions for sintered parts. 3 sintered tensile bars were tested and saw an average Elastic Modulus of 10,245 MPa, Yield Stress of 59 MPa, and Ultimate Tensile Strength of 153 MPa. In future mechanical property testing of parts printed with the 17-4 PH stainless-steel material, there will be an increase of 20% in all directions to account for the shrinkage, as the tensile bars in this initial testing were not oversized in printing.

However, these initial results prove the concept of using the 17-4 PH stainless-steel filament material in the MF³ process and outline successful printing parameters with initial density, shrinkage, and mechanical property measurements to improve upon in future tests.

In addition to printing with the stainless-steel filaments, work was done on redesigning parts commonly manufactured via conventional machining methods (Monticello Tool & Die, Monticello, KY, USA). Parts sampled from the outside machine shop were redesigned using topology optimization methods, applying simple lattice structures on the outside surfaces and infills. This design method is commonly used in Additive Manufacturing and is beneficial when used in MF³, as it can save part mass while still satisfying mechanical property requirements and reduce printing time and material usage. FIGURE 28 shows 4 parts that were redesigned via topology optimization, with the first 3 having the lattice design applied to the outside surface and the 4th having the lattice design applied to the infill. In future work, these parts can be printed with the 17-4 PH stainless-steel or aluminum-6061 materials to confirm dimensional tolerance and functionality of the parts after sintering.

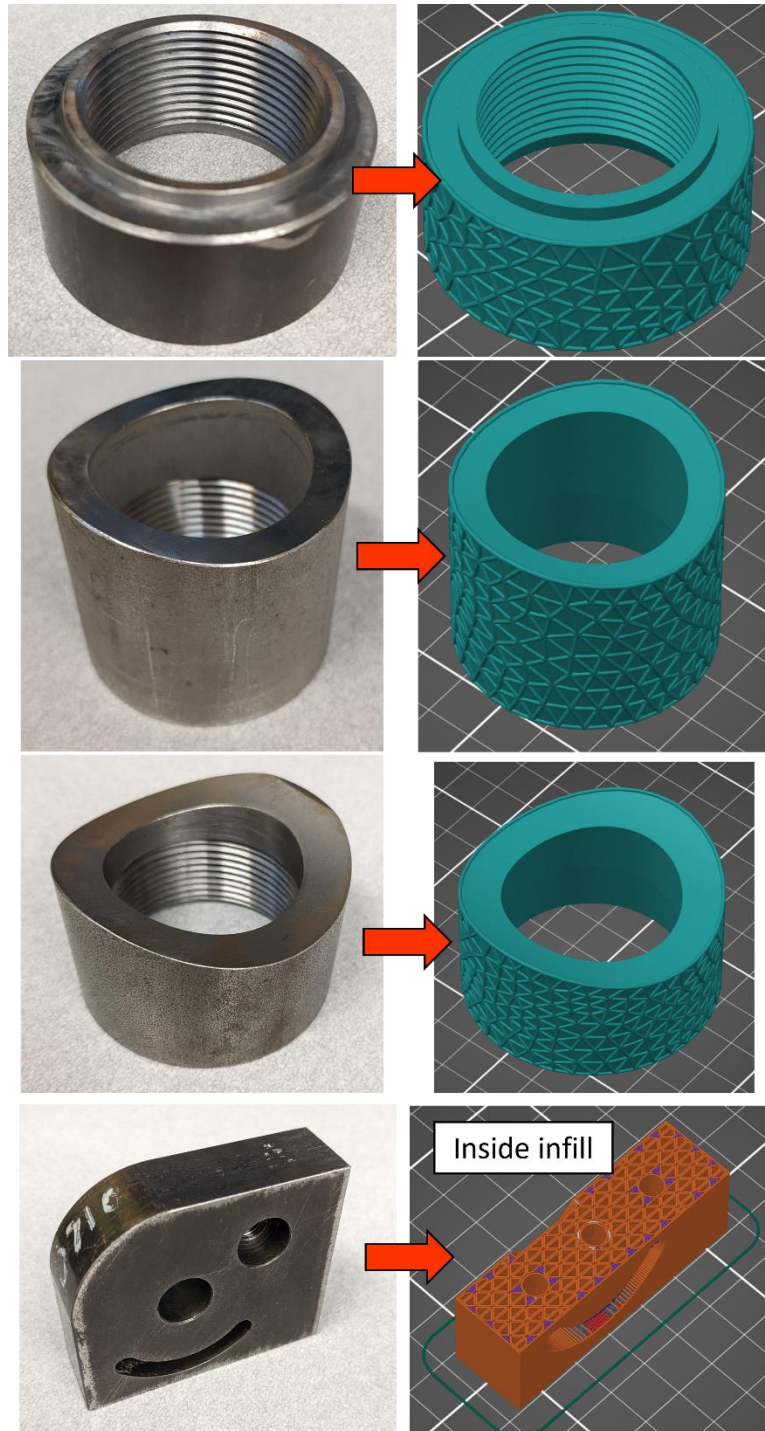


FIGURE 28 - Redesigned parts using topology optimization technique for future printing

APPENDIX II. MF³ OF WC-Co

In this work, a tungsten carbide-cobalt (WC-Co) sample of powder was received (Global Tungsten & Powders, Towanda, PA, USA) and applied in the first steps of the Metal Fused Filament Fabrication (MF³) process. An SEM image, shown in FIGURE 29 shows the mostly spherical nature of the powder particles with the approximate size of 150 μm . The pycnometer density of the powder was measured to be 11.06 g/cm^3 , and two feedstock batches were mixed. The first batch was measured at 25 vol% (79 weight %) of the WC-Co powder and the second batch was mixed at 50 vol% (92 weight %). Thermogravimetric analysis (TGA) tests were performed for both feedstock samples, with the resulting change in weight graphs shown in FIGURE 30, showing relatively the same thermal behavior where the polymer binder would be degraded. Filaments at both solids loadings were extruded from pelletized feedstock samples. Only the filament at the lower solids loading (25 vol%) was able to be used in successful green printing. The

filament at 50 vol% was more brittle than the 25 vol% filament, breaking too easily in the printer's extruder. 10 mm x 10 mm tablets were printed using a 210 °C nozzle temperature, 10 mm/s print speed, 0.3 mm layer thickness, 0.8 mm extrusion width with a 0.8 mm-diameter hardened steel nozzle, 45 ° infill, 80 °C bed temperature, and 1.0 Extrusion Multiplier. The average density of the green parts was 2.59 g/cm³ at 69.37 % relative density compared to the filament (3.73 g/cm³). A printed part is shown in FIGURE 31, with the gaps between layers that lead to lower green density being visible.

The Optimum Solids Loading can be determined in future experiments, as there were only two points selected in initial feedstock filament production (25 vol% and 50 vol%) . Future filaments can be produced at the Optimum Solids Loading to enable more successful printing. More work is needed to refine the printing parameters to print fully dense green parts. Once the optimized printing is realized, debinding and sintering tests may be conducted using initial TGA test data to form fully dense, pure WC-Co parts.

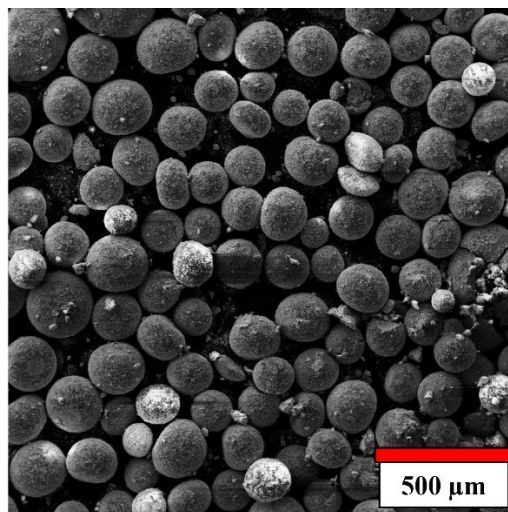


FIGURE 29 - WC-Co powder SEM image

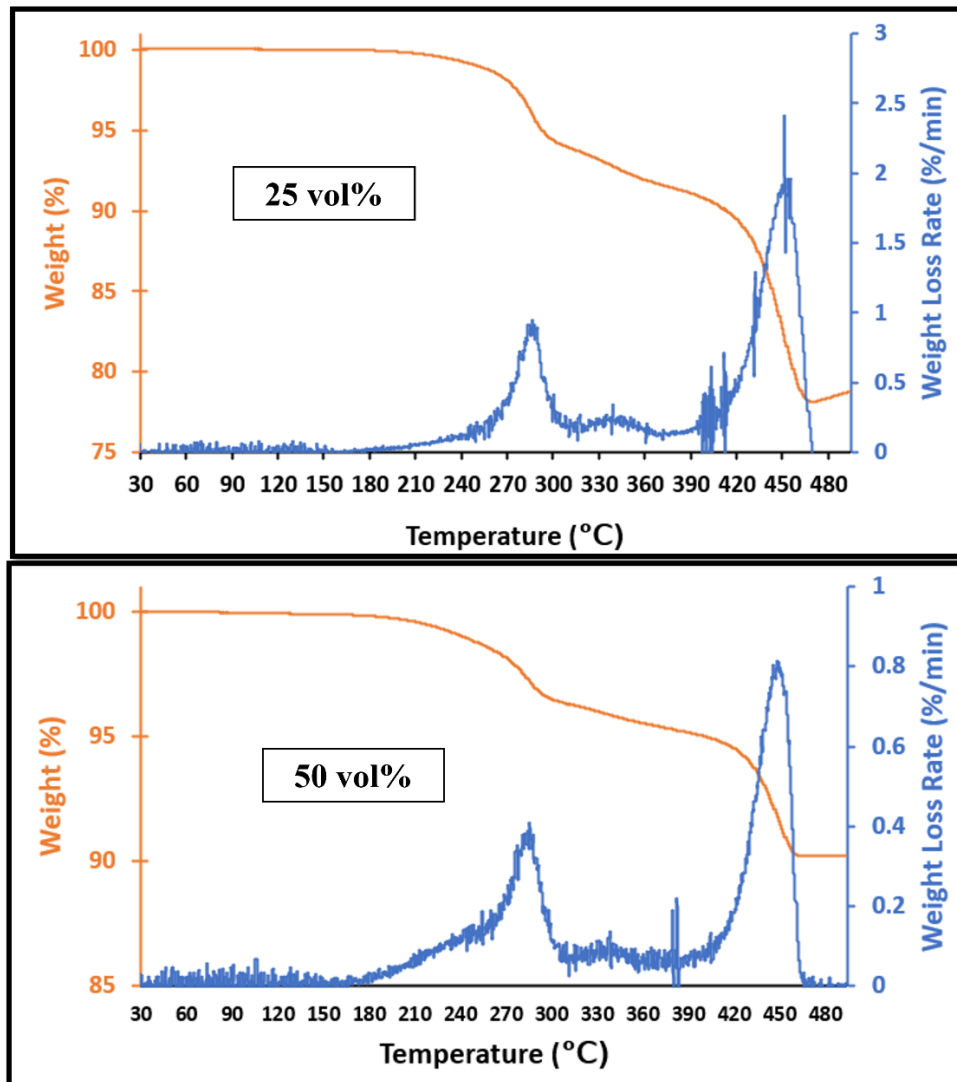


FIGURE 30 - TGA results of WC-Co feedstocks

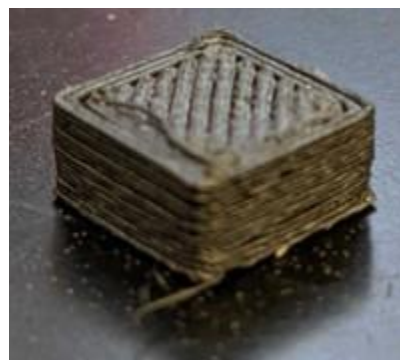


FIGURE 31 - Printed WC-Co green part at 25 vol% solids loading

LIST OF REFERENCES

- Arockiasamy, A., German, R. M., Wang, P. T., Horstemeyer, M. F., Morgan, W., Park, S. J., & Otsuka, I. (2011). Sintering behaviour of Al-6061 powder produced by rapid solidification process. *Powder Metallurgy*, *54*(3), 354–359.
<https://doi.org/10.1179/003258909X12573447241626>
- ASM Aerospace Specification Metals Inc. (n.d.). *ASM Material Data Sheet*. Retrieved from <https://asm.matweb.com/search/SpecificMaterial.asp?bassnum=ma6061t6>.
- Chen, H., Sun, Q., Tian, T., Zheng, L., Barré, M., Monot-Laffez, I., Makowska-Janusik, M., Li, G., & Kassiba, A. H. (2020). Defects and microstructure of highly conducting Al-doped ZnO ceramics obtained via spark plasma sintering. *Journal of the European Ceramic Society*, *40*(15), 5529–5534.
<https://doi.org/10.1016/j.jeurceramsoc.2020.06.030>
- Ding, H., Zeng, C., Raush, J., Momeni, K., & Guo, S. (2022). Developing Fused Deposition Modeling Additive Manufacturing Processing Strategies for Aluminum Alloy 7075: Sample Preparation and Metallographic Characterization. *Materials*, *15*(4). <https://doi.org/10.3390/ma15041340>
- Ernst, A. T., Kerns, P., Nardi, A., Brody, H. D., Dongare, A. M., Lee, S.-W., Champagne, V. K., Suib, S. L., & Aindow, M. (2020). *Surface States of Gas-Atomized Al 6061 Powders-Effects of Heat Treatment*.
- Fang, Z. Zak. (2010). *Sintering of advanced materials : fundamentals and processes*. Woodhead Pub.
- German, R. M. (n.d.). *Sintering : from empirical observations to scientific principles*.
- German, R. M., & Metal Powder Industries Federation. (2011). *Metal injection molding : a comprehensive MIM design guide*. Metal Powder Industries Federation.
- Godec, D., Cano, S., Holzer, C., & Gonzalez-Gutierrez, J. (2020). Optimization of the 3D printing parameters for tensile properties of specimens produced by fused filament fabrication of 17-4PH stainless steel. *Materials*, *13*(3).
<https://doi.org/10.3390/ma13030774>
- Gürbüz, M., Can Şenel, M., & Koç, E. (2018). The effect of sintering time, temperature, and graphene addition on the hardness and microstructure of aluminum composites. *Journal of Composite Materials*, *52*(4), 553–563.
<https://doi.org/10.1177/0021998317740200>
- Jiang, J., Chen, P., Qiu, J., Sun, W., Chizhik, S. A., Makhaniok, A. A., Melnikova, G. B., & Kuznetsova, T. A. (2021). The effect of heating rate on the sintering of aluminum

- nanospheres. *Physical Chemistry Chemical Physics*, 23(20), 11684–11697.
<https://doi.org/10.1039/d0cp06669a>
- José, F., Instituto, C., Nunes, P., Silva, A., Vieira, M.-T. F., Barreiros, F. M., & Cerejo, F. (n.d.). *Fused Deposition of WC+Co powder HYRONMAN: HYBRID ROBOTIC ADDITIVE MANUFACTURING PLATFORM FOR AGILE PRODUCTION OF LARGE LIGHTWEIGHT COMPONENTS* View project PAMI-Portuguese Additive Manufacturing Initiative View project Fused Deposition of WC+Co powder.
<https://www.researchgate.net/publication/336771325>
- Kent, D., Qian, M., & Schaffer, G. B. (2010). Formation of aluminium nitride during sintering of powder injection moulded aluminium. *Powder Metallurgy*, 53(2), 118–124. <https://doi.org/10.1179/003258909X12523294330154>
- Liu, Z. Y., Sercombe, T. B., & Schaffer, G. B. (2007). The effect of particle shape on the sintering of aluminum. *Metallurgical and Materials Transactions A: Physical Metallurgy and Materials Science*, 38(6), 1351–1357.
<https://doi.org/10.1007/s11661-007-9153-2>
- Lu, J., Zhou, Y., Zheng, Y., Li, S., Huang, Z., & Zhai, H. (2012). Effects of sintering process on the properties of Ti₃SiC₂/Cu composite. *Key Engineering Materials*, 512–515, 377–381. <https://doi.org/10.4028/www.scientific.net/KEM.512-515.377>
- Lumley, R. N., Sercombe, T. B., & Schaffer, G. B. (1999). *Surface Oxide and the Role of Magnesium during the Sintering of Aluminum* (Vol. 30).
- Mendoza, J., Carreño-Gallardo, C., Estrada-Guel, I., Garay-Reyes, C. G., Ruiz-Esparza-Rodríguez, M. A., Rodríguez-Cabiales, G., Guía-Tello, J. C., & Martínez-Sánchez, R. (2021). Effect of the route and sintering time in the microstructure of pure aluminum prepared by high energy ball milling. *Microscopy and Microanalysis*, 27(S1), 3294–3296. <https://doi.org/10.1017/s143192762101134x>
- Pazhamannil, R. V., Jishnu Namboodiri, V. N., Govindan, P., & Edacherian, A. (2022). Property enhancement approaches of fused filament fabrication technology: A review. In *Polymer Engineering and Science*. John Wiley and Sons Inc.
<https://doi.org/10.1002/pen.25948>
- Schaffer, G. B., & Hall, B. J. (n.d.). *The Influence of the Atmosphere on the Sintering of Aluminum*.
- Schaffer, G. B., Hall, B. J., Bonner, S. J., Huo, S. H., & Sercombe, T. B. (2006). The effect of the atmosphere and the role of pore filling on the sintering of aluminium. *Acta Materialia*, 54(1), 131–138. <https://doi.org/10.1016/j.actamat.2005.08.032>

- Schaffer, G. B., Sercombe, T. B., & Lumley, R. N. (2001). Liquid phase sintering of aluminium alloys. In *Materials Chemistry and Physics* (Vol. 67).
- Schneidler, J., Berry, C., & Barari, A. (2021). Improving 3D printing geometric accuracy using design of experiments on process parameters in fused filament fabrication (FFF). *2021 14th IEEE International Conference on Industry Applications, INDUSCON 2021 - Proceedings*, 1360–1365. <https://doi.org/10.1109/INDUSCON51756.2021.9529615>
- Singh, P., Balla, V. K., Atre, S. v., German, R. M., & Kate, K. H. (2021). Factors affecting properties of Ti-6Al-4V alloy additive manufactured by metal fused filament fabrication. *Powder Technology*, 386, 9–19. <https://doi.org/10.1016/j.powtec.2021.03.026>
- Singh, P., Balla, V. K., Gokce, A., Atre, S. v., & Kate, K. H. (2021). Additive manufacturing of Ti-6Al-4V alloy by metal fused filament fabrication (MF3): producing parts comparable to that of metal injection molding. *Progress in Additive Manufacturing*, 6(4). <https://doi.org/10.1007/s40964-021-00167-5>
- Singh, P., Balla, V. K., Tofangchi, A., Atre, S. v., & Kate, K. H. (2020). Printability studies of Ti-6Al-4V by metal fused filament fabrication (MF3). *International Journal of Refractory Metals and Hard Materials*, 91. <https://doi.org/10.1016/j.ijrmhm.2020.105249>
- Soares, E., Bouchonneau, N., Alves, E., Alves, K., Filho, O. A., Mesguich, D., Chevallier, G., Laurent, C., & Estournès, C. (2021). Microstructure and mechanical properties of AA7075 aluminum alloy fabricated by spark plasma sintering (SPS). *Materials*, 14(2), 1–11. <https://doi.org/10.3390/ma14020430>
- Thompson, Y., Gonzalez-Gutierrez, J., Kukla, C., & Felfer, P. (2019). Fused filament fabrication, debinding and sintering as a low cost additive manufacturing method of 316L stainless steel. *Additive Manufacturing*, 30. <https://doi.org/10.1016/j.addma.2019.100861>
- Uddin, S. Z., Murr, L. E., Terrazas, C. A., Morton, P., Roberson, D. A., & Wicker, R. B. (2018). Processing and characterization of crack-free aluminum 6061 using high-temperature heating in laser powder bed fusion additive manufacturing. *Additive Manufacturing*, 22, 405–415. <https://doi.org/10.1016/j.addma.2018.05.047>
- Wagner, M. A., Hadian, A., Sebastian, T., Clemens, F., Schweizer, T., Rodriguez-Arbaizar, M., Carreño-Morelli, E., & Spolenak, R. (2022). Fused filament fabrication of stainless steel structures - from binder development to sintered properties. *Additive Manufacturing*, 49. <https://doi.org/10.1016/j.addma.2021.102472>

- Wang, T., Yang, L., Ma, Y., Wu, L., Yan, H., Liu, W., Liu, C., & Huang, Y. (2021). Microstructure and Mechanical Properties of 7055 Al Alloy Prepared by Hot-Press Sintering of Powder Byproduct and Optimization of Sintering Parameters. *JOM*, 73(9), 2615–2624. <https://doi.org/10.1007/s11837-021-04768-x>
- Wu, L., Yu, Z., Liu, C., Ma, Y., Huang, Y., Wang, T., Yang, L., Yan, H., & Liu, W. (2021). Microstructure and tensile properties of aluminum powder metallurgy alloy prepared by a novel low-pressure sintering. *Journal of Materials Research and Technology*, 14, 1419–1429. <https://doi.org/10.1016/j.jmrt.2021.07.074>
- Yang, D., Tian, Z., Song, J., Lu, T., Qiu, G., Kang, J., Zhou, H., Mao, H., & Xiao, J. (2021). Influences of sintering temperature on pore morphology, porosity, and mechanical behavior of porous Ti. *Materials Research Express*, 8(10). <https://doi.org/10.1088/2053-1591/ac1b63>

CURRICULUM VITA

NAME: Luke Malone

ADDRESS: 2400 Mellwood Avenue, Apt. 1321, Louisville, KY 40206

CONTACT: (502) 648-9010, luke.malone@louisville.edu

EDUCATION: B.S., Mechanical Engineering, University of Louisville (2017-21)

M.ENG., Mechanical Engineering University of Louisville (2021-22)

AWARDS: 2021 J. B. Speed School Leader of the Year Award

NASA Kentucky Space Grant Consortium and EPSCoR Programs Graduate
Student Fellowship – Space Grant award

International Conference on Injection Molding of Metals, Ceramics and Carbides
2022 - grant recipient/presenter

Conn Center for Renewable Energy Nobel Laureate 2022 event presenter

Additive Manufacturing with Powder Metallurgy 2022 - NSF grant
recipient/presenter